

Low-latitude climate change linked to high-latitude glaciation during the Late Paleozoic Ice Age

Zhang, Peixin; Yang, Minfang; Lu, Jing; Shao, Longyi; Wang, Ziwei ; Hilton, Jason

DOI:

[10.3389/feart.2022.95686](https://doi.org/10.3389/feart.2022.95686)

License:

Creative Commons: Attribution (CC BY)

Document Version

Publisher's PDF, also known as Version of record

Citation for published version (Harvard):

Zhang, P, Yang, M, Lu, J, Shao, L, Wang, Z & Hilton, J 2022, 'Low-latitude climate change linked to high-latitude glaciation during the Late Paleozoic Ice Age: evidence from terrigenous detrital kaolinite', *Frontiers in Earth Science*. <https://doi.org/10.3389/feart.2022.95686>

[Link to publication on Research at Birmingham portal](#)

General rights

Unless a licence is specified above, all rights (including copyright and moral rights) in this document are retained by the authors and/or the copyright holders. The express permission of the copyright holder must be obtained for any use of this material other than for purposes permitted by law.

- Users may freely distribute the URL that is used to identify this publication.
- Users may download and/or print one copy of the publication from the University of Birmingham research portal for the purpose of private study or non-commercial research.
- User may use extracts from the document in line with the concept of 'fair dealing' under the Copyright, Designs and Patents Act 1988 (?)
- Users may not further distribute the material nor use it for the purposes of commercial gain.

Where a licence is displayed above, please note the terms and conditions of the licence govern your use of this document.

When citing, please reference the published version.

Take down policy

While the University of Birmingham exercises care and attention in making items available there are rare occasions when an item has been uploaded in error or has been deemed to be commercially or otherwise sensitive.

If you believe that this is the case for this document, please contact UBIRA@lists.bham.ac.uk providing details and we will remove access to the work immediately and investigate.



OPEN ACCESS

EDITED BY

Idoia Rosales,
CN Instituto Geológico y Minero de
España (CSIC), Spain

REVIEWED BY

Miguel Ángel Caja Rodríguez,
Repsol, Spain
Neil Griffiths,
United States Geological Survey,
United States

*CORRESPONDENCE

Jing Lu,
lujing@cumtb.edu.cn

SPECIALTY SECTION

This article was submitted to
Sedimentology, Stratigraphy and
Diagenesis,
a section of the journal
Frontiers in Earth Science

RECEIVED 30 May 2022

ACCEPTED 19 July 2022

PUBLISHED 26 August 2022

CITATION

Zhang P, Yang M, Lu J, Shao L, Wang Z
and Hilton J (2022), Low-latitude
climate change linked to high-latitude
glaciation during the late paleozoic ice
age: Evidence from terrigenous
detrital kaolinite.
Front. Earth Sci. 10:956861.
doi: 10.3389/feart.2022.956861

COPYRIGHT

© 2022 Zhang, Yang, Lu, Shao, Wang
and Hilton. This is an open-access
article distributed under the terms of the
[Creative Commons Attribution License
\(CC BY\)](https://creativecommons.org/licenses/by/4.0/). The use, distribution or
reproduction in other forums is
permitted, provided the original
author(s) and the copyright owner(s) are
credited and that the original
publication in this journal is cited, in
accordance with accepted academic
practice. No use, distribution or
reproduction is permitted which does
not comply with these terms.

Low-latitude climate change linked to high-latitude glaciation during the late paleozoic ice age: Evidence from terrigenous detrital kaolinite

Peixin Zhang¹, Minfang Yang², Jing Lu^{1*}, Longyi Shao¹,
Ziwei Wang¹ and Jason Hilton³

¹State Key Laboratory of Coal Resources and Safe Mining, College of Geoscience and Surveying Engineering, China University of Mining and Technology, Beijing, China, ²Research Institute of Petroleum Exploration and Development, PetroChina, Beijing, China, ³School of Geography, Earth and Environmental Sciences, The University of Birmingham, Birmingham, United Kingdom

The Late Paleozoic Ice Age (LPIA; ca. 335–260 million years ago) was one of the most significant glacial events in Earth's history. It records cycles of ice advance and retreat in southern high-latitude Gondwana and provides a deep-time perspective for climate–glaciation coevolution. However, climate records using clay mineral proxies from the LPIA are poorly developed in low latitudes, particularly in the North China Plate (NCP) on the eastern Paleo-Tethys. We address this through a detailed mineralogical study of the marine–continental sedimentary succession in the Yuzhou Coalfield from the southern NCP. We apply biostratigraphy and high-resolution clay mineral composition to reconstruct the latest Carboniferous to early Permian chronostratigraphy and climate change. The Benxi, Taiyuan, and Shanxi formations in the study area are assigned to the Gzhelian, Asselian–Artinskian, and Kungurian–Roadian stages, respectively, and the Carboniferous and Permian lithostratigraphic units across the NCP recognized as widely diachronous. Under scanning electron microscopy, the detrital micromorphology of kaolinite is mostly found as irregular fragments with sizes of 1–5 μm . Illite crystallization varies from 0.22 to 1.88 $\Delta^\circ/2\theta$ (\bar{x} = 0.49 $\Delta^\circ/2\theta$) and indicates changes in kaolinite content to be a robust proxy for paleoclimate reconstruction. Kaolinite data show alternating warm-humid and cool-humid climate conditions that are roughly consistent with the calibrated glaciations and nonglacial interval successions recognized in high-latitude Gondwana. These include the Asselian-early Sakmarian and late Sakmarian-early Artinskian glacials and the climatic transition to glacial P3 during the Roadian. Our results indicate a comparatively cool-humid and warm-humid climate mode in low-latitude NCP during glacial and nonglacial periods, respectively. This is a significant step toward connecting climate change in low-latitude to high-latitude glaciation during the LPIA in eastern Paleo-Tethys.

KEYWORDS

high-latitude glaciation, clay minerals, terrigenous detrital kaolinite, paleoclimate, low-latitudes, north China

1 Introduction

The Cisuralian (early Permian) represents the peak of the late paleozoic ice age (LPIA; *ca.* 335–260 Ma) in which significant shifts between glacial to nonglacial conditions occurred in high-latitude Gondwana (e.g., [Montañez et al., 2007](#); [Fielding et al., 2008a, 2008b, 2008c](#); [Frank et al., 2008a, 2008b](#); [Montañez and Poulsen, 2013](#); [Griffis et al., 2018, 2019, 2021](#); [Fedorchuk et al., 2019a, 2019b](#); [Garbelli et al., 2019](#); [Richey et al., 2020](#)). These glaciations and nonglacial events caused fluctuations in the global climate and are recorded by indirect proxies (e.g., $\delta^{18}\text{O}$, $\delta^{13}\text{C}$, foraminifera fossil, and CIA values) from mid- and low-latitudes in marine and continental deposits ([Korte et al., 2005](#); [Frank et al., 2008a](#); [Grossman et al., 2008](#); [Davydov et al., 2014](#); [Yang et al., 2016, 2020](#); [Lu et al., 2021a, 2021c](#)) and shallow marine fossil data in high latitudes of the Northern Hemisphere ([Davydov and Biakov, 2015](#)). However, records of glaciations and nonglacial-induced climate changes at low latitudes are different in western and eastern Tethys. In western Tethys and mid-continental Euramerica, previous studies of paleosols, evaporites, flora, and sedimentology reveal semi-arid to arid climates during the Early Permian deglaciation ([Tabor and Montañez, 2002](#); [Tabor et al., 2008](#); [Bishop et al., 2010](#); [DiMichele et al., 2010](#); [DiMichele, 2014](#); [Michel et al., 2015](#)). By contrast, in the eastern Tethys, the widespread distribution of tropical peat-forming wetland plant communities implies warm and wet environments persisted, including those across the North China Plate (NCP) ([Hilton and Cleal, 2007](#); [Tabor et al., 2008](#); [Wang, 2010](#); [Wang and Pfefferkorn, 2013](#)). Therefore, the paleoclimate study of the NCP in eastern Tethys is of great significance for understanding the global effects of high-latitude glaciations and nonglacial rhythms during the LPIA.

The kaolinite content of mudrock is an important climate proxy and has been widely used to reconstruct paleoclimatic change over different timescales ([Singer, 1984](#); [Frings, 2019](#)). Previous studies have demonstrated kaolinite as a product of weathering which is controlled by climatic factors (mainly temperature and humidity), with paleoclimatic information from kaolinite typically agreeing with conclusions from other climate proxies in marine and continental deposits, including paleopalynology and oxygen-isotope analysis ([Singer, 1984](#); [Frings, 2019](#)). Although clay mineral composition (e.g., kaolinite and illite) is an important climate proxy that has been successfully used to reconstruct past climate conditions from eastern Paleo-Tethys ([Cheng et al., 2019](#); [Lu et al., 2020](#)), few studies have considered paleoclimates from clay mineral proxies linked to glacial events during the early Permian.

In this article, we use revised conodont biostratigraphy and previous fusulinid and plant megafossil biostratigraphy and lithostratigraphy ([Wang and Shang, 1989](#); [Wang and Qi, 2003](#); [Pei, 2004, 2009](#); [Gao et al., 2005](#); [Yang and Wang, 2012](#))

to constrain the age of the studied strata in the Yuzhou Coalfield of the southern NCP and enable its correlation with well-dated glaciations. We use the clay mineral kaolinite as a proxy to reconstruct paleoclimate and reveal the links between low-latitude climate change and high-latitude glaciation during the late Pennsylvanian-earliest Guadalupian. This provides significant insights into low-latitude signals for climate change during the LPIA.

2 Geological setting

During the early Permian, the Yuzhou Coalfield (study area) in the NCP was located at approximately 11.0–11.4°N on the northern margin of the Paleo-Tethys Ocean (PTO) ([Supplementary Table S1](#)) ([Zhu et al., 1996](#)). Previous analysis of paleocurrent and paleogeography shows that during the Permian, the NCP was higher in the north and lower in the south ([Yang and Lei, 1987](#); [Shang, 1997](#)). Sediments were mainly derived from the Inner Mongolia Uplift (IMU) in the northern part of the NCP following the ongoing southerly subduction of the Paleo-Asian Ocean beneath the NCP ([Yang and Lei, 1987](#); [Liu, 1990](#)). Lithologies in the IMU source area mainly comprise Archean gneiss and granulite and less frequent Archean granite and Proterozoic sedimentary rocks ([Zhou, 2002](#)).

The lithostratigraphic units studied in this article include the Benxi (= Penchi), Taiyuan, and Shanxi (= Shansi) formations in increasing order. In Henan Province in the southern NCP ([Figures 1A,B](#)), the target strata unconformably overlie Ordovician gray-black marine limestones and contact conformably with the overlying Xiashihezi Formation ([Yang and Lei, 1987](#); [Yang, 2006](#)). The Benxi Formation comprises three members in Henan Province ([Figure 1C](#)) ([Pei, 2009](#)), but only the upper member is developed in the study area where it mainly comprises gray-white iron and aluminum-rich mudrocks ([Figure 1C](#)) ([Yang, 2006](#); [Pei, 2009](#)). The Taiyuan Formation includes the Dajian, Mojie, and Zhutougou members in ascending order and comprises mainly terrigenous mudrock and marine limestone beds (numbered #L₁ to #L₉) with one regionally extensive, thick layer of sandstone (the Hushi sandstone) and some thin coal seams ([Figure 1C](#)) ([Yang, 2006](#); [Pei, 2009](#)).

In the Shanxi Formation, the basal #2₁ Coal Member includes the economically important #2₁ coal seam and is dominated mainly by grayish-black mudrocks ([Figure 1C](#)) ([Yang, 2006](#); [Pei, 2009](#)). The Dazhan and Xiangtan Sandstone (DZ and XT) members ([Figure 1C](#)) of the Shanxi Formation mainly encompass gray, fine-medium sandstone, and gray mudrocks with thin coal seams. The DZ and XT Sandstone members were deposited as distributary channels or river mouth bars in a deltaic setting and constitute regional lithostratigraphic marker beds that crop through Henan Province ([Yang and Lei, 1987](#)). At the

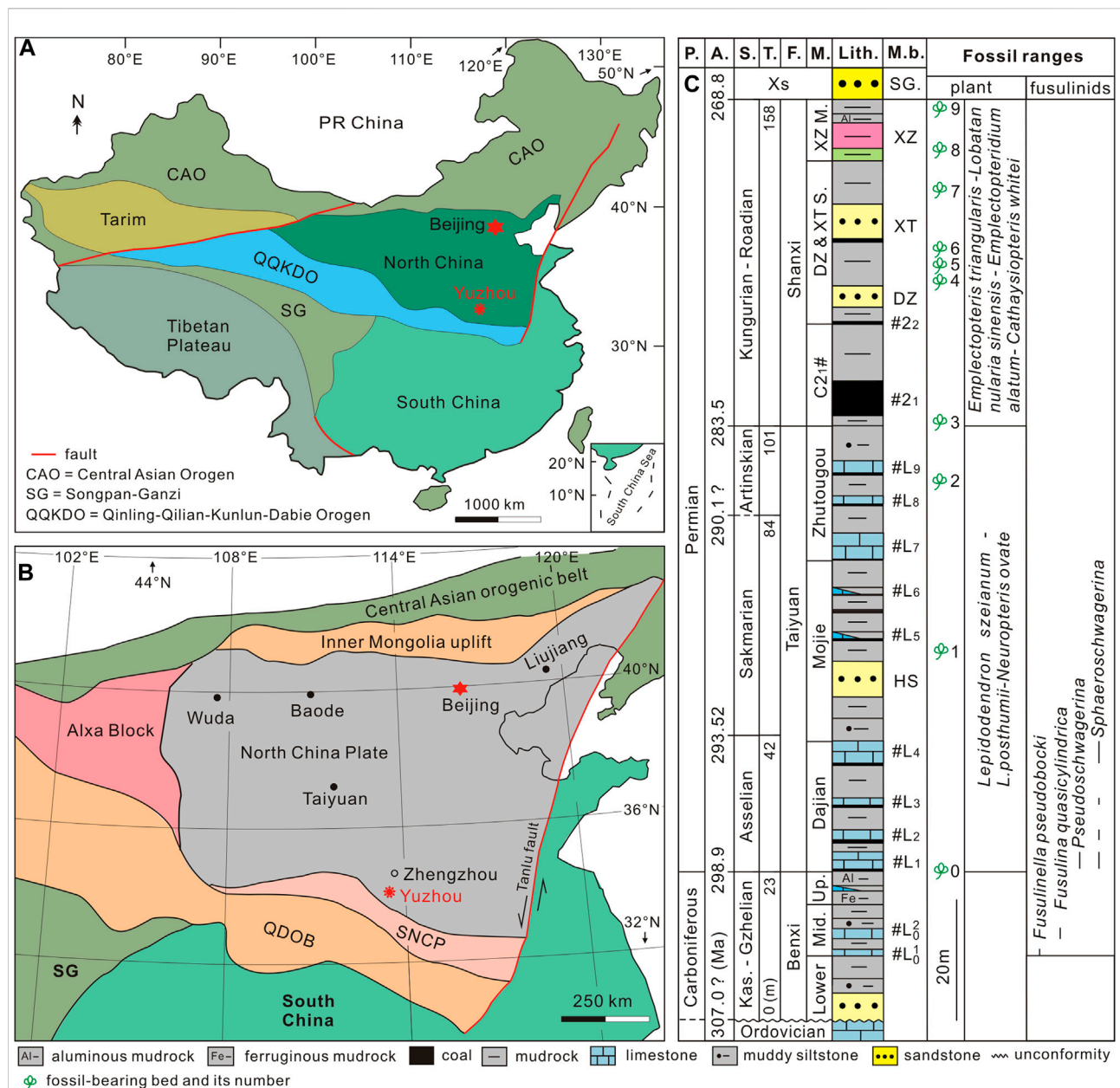
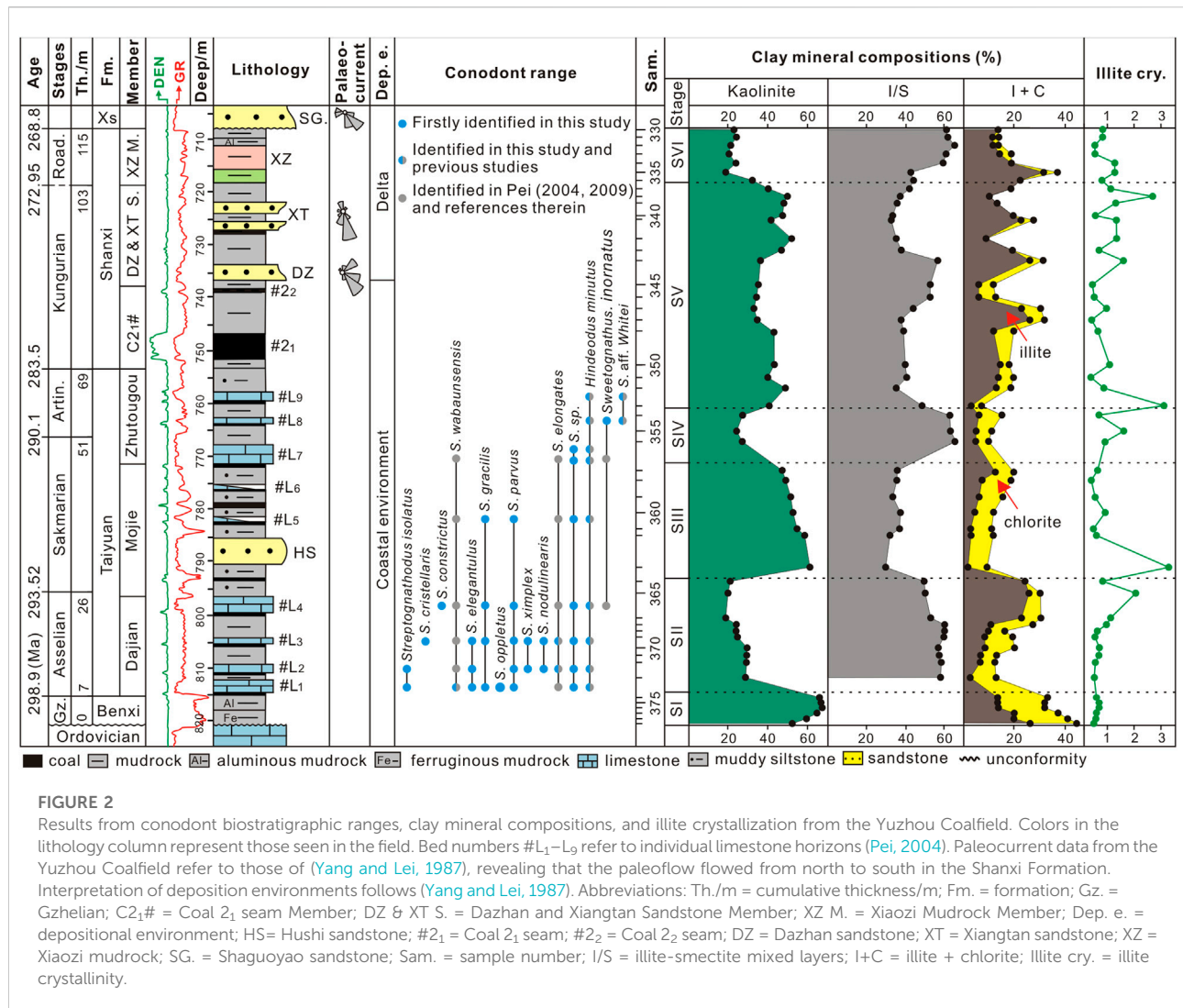


FIGURE 1

Location and geological context for the study area. (A) Generalized tectonic map of present-day China showing the location of the North China Plate (NCP) and the study area (modified from (Lu et al., 2020)). (B) Simplified tectonic map of the present-day NCP showing the location of the study area (modified from (Lu et al., 2021c)). (C) Stratigraphic framework and fossil distributions for the studied Carboniferous-Permian strata of the Benxi, Taiyuan, Shanxi, and Xiashihezi (Xs) formations from Henan Province in the southern NCP. Lithology column derived from (Pei, 2004) and (Yang, 2006) with colors representing those of the strata in the field (Section 2). L₀¹ to L₉ represent the position of individual limestone marker beds. Fossil plant assemblages (0–9) from (Yang, 2006) and (Yang and Wang, 2012). Fusulinid stratigraphic ranges and biozones from (Pei, 2004, 2009). Abbreviations: SG = Songpan-Ganzi Terrane; QDOB = Qingling-Dabie orogenic belt; SNCP = south North China Plate; P. = period; S. = stages; Kas. = Kasimovian; T. = cumulative thickness; F. = formation; M. = member; C₂₁# = Coal 2₁ seam member; DZ & XT S. = Dazhan and Xiangtan Sandstone Member; XZ M. = Xiaozhi Mudrock Member; Mid. = middle; Up. = upper; Lith. = Lithology; M.b. = marker bed; HS = Hushi sandstone; 2₁# = Coal 2₁ seam; DZ = Dazhan sandstone; XT = Xiangtan sandstone; XZ = Xiaozhi mudrock; SG. = Shaguoyao sandstone.

top of the Shanxi Formation, the Xiaozhi Mudrock Member (XZ M.) (Figure 1C) comprises purplish-red and grayish-green mudrock deposited in delta plain environments and lacks

coals. The Xiaozhi Member also represents an important regional lithostratigraphic marker (Figure 1C) (Yang and Lei, 1987).



3 Materials and methods

From the ZK21-1 borehole (34°18'3"N, 113°20'13"E) in the Yuzhou Coalfield, fresh mudrock (50 samples) was collected from the Benxi to the Shanxi formations (sampling locations shown in Figure 2). Samples were ground to less than 200 μm using mesh sieves and divided into three subparts for the analysis of 1) clay mineral composition, 2) major element content, and 3) trace element content. Clay mineral composition was analyzed using an X-ray diffractometer (D/max 2500 PC) at the State Key Laboratory of Coal Resources and Safe Mining (Beijing), and the data were interpreted using Clayquan 2016 software, with a relative analysis error of $\pm 5\%$. At the Beijing Research Institute of Uranium Geology, major and trace element analyses were undertaken using an X-ray fluorescence spectrometer (PW2404, relative analysis error of $\pm 5\%$) and an inductively coupled plasma mass spectrometer (Finnigan MAT, relative analysis error of $\pm 5\%$), respectively, and the

micromorphology of kaolinite was observed under scanning electron microscopy (SEM, FEI Nova Nano SEM450) with an energy-dispersive spectrometer (Oxford instrument X-Max80 detector).

A total of nine fresh limestone samples were collected for conodont biostratigraphy from the Taiyuan Formation (sampling locations shown in Figure 2); it was not possible to collect from the #L₆ limestone because no exposed strata were observed in the field. Conodont samples were crushed to <5 mm pieces and dissolved in a solution of 6–10% acetic acid that was buffered with tricalcium phosphate. The acid and buffer were exchanged every 48 h until the samples were fully dissolved. Residual materials were wet sieved, dried at 50°C, and separated for heavy fractions using sodium polytungstate. Conodont elements were picked under a binocular microscope at the State Key Laboratory Geological Processes and Mineral Resources (Beijing).

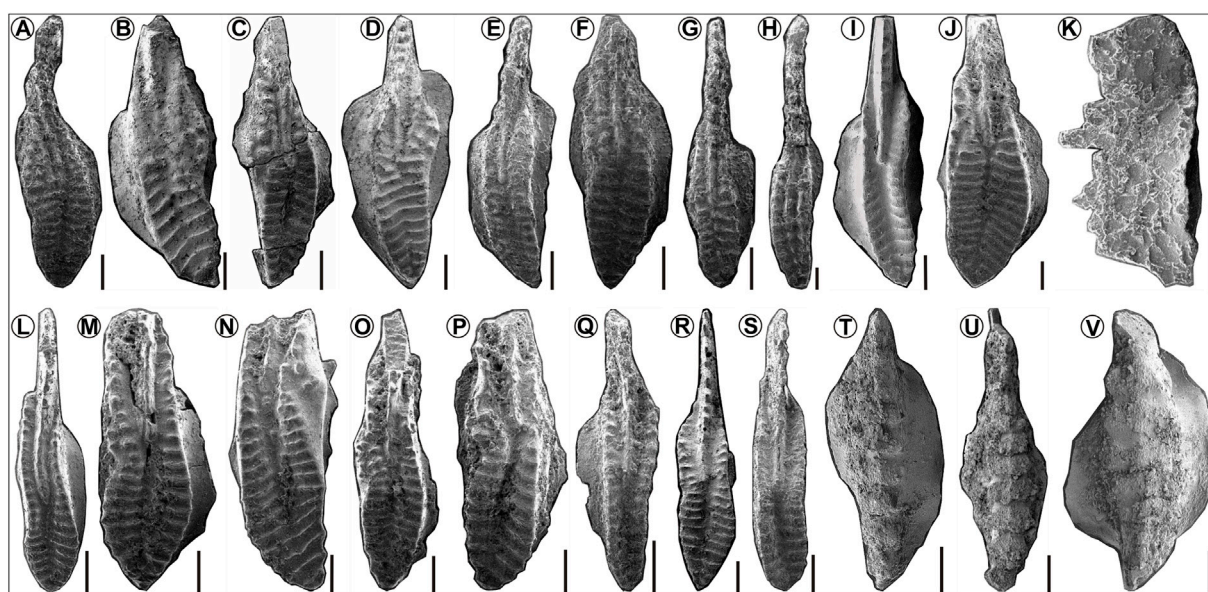


FIGURE 3

SEM images of example conodonts from limestones #L₁, #L₂, #L₃, #L₄, and #L₈ in the study area (all scale bars = 100 μ m). (A–C), *Streptognathodus isolatus* (#L₁ and #L₂) (D), *Streptognathodus wabaunsensis* (#L₁) (E), *Streptognathodus elegantulus* (#L₁) (F), *Streptognathodus gracilis* (#L₁) (G), *Streptognathodus oppletus* (#L₁) (H), *Streptognathodus parvus* (#L₁) (I), *Streptognathodus ximplex* (#L₂) (J), *Streptognathodus nodulinear* (#L₂) (K), *Hindeodus minutus* (#L₁) (L), *Streptognathodus elongates* (#L₂) (M–P), *Streptognathodus cristellaris* (#L₃) (Q) and (R), *Streptognathodus constrictus* (#L₄) (S), *Streptognathodus cf. constrictus* (#L₄) (T) and (U), *Sweetognathus aff. whitei* (#L₈) (V), and *Sweetognathus inornatus* (#L₈).

The abundance of kaolinite in modern sediments is dependent on the intensity of chemical weathering controlled by climate (Singer, 1984; Thiry, 2000). As kaolinite has strong resistance to diagenesis, changes in the terrigenous kaolinite content of clay minerals in this study were used to reconstruct paleoclimatic change in the target strata. The influence of depositional recycling, hydraulic sorting, and post-deposition diagenesis can affect kaolinite content, so these have been evaluated by analysis of Th/U ratios, correlation analysis of Al/Si ratios, K/Si ratios, Weathering Index of Parker (WIP), and illite crystallinity (KI) and kaolinite micromorphology of under SEM (Chen et al., 2003; Bauluz et al., 2008; Roy and Roser, 2013; Yang et al., 2016, 2018; Cheng et al., 2019).

4 Results and analysis

4.1 Conodonts

A total of 28 species of conodonts have been identified in the sampled limestones from the studied strata (Figures 2, 3; Supplementary Table S2). Among them, the first occurrence (FO) of *Streptognathodus isolatus* in limestone #L₁ occurs at the base of the Asselian stage (Figures 2, 3A–C; Supplementary

Table S2) and defines the Carboniferous–Permian (C–P) boundary (Wang, 1991; Wang and Qi, 2003; Shen et al., 2019). The FO of *Streptognathodus cristellaris* in limestone #L₃ (Figures 2, 3M–P; Supplementary Table S2) and *Streptognathodus constrictus* in limestone #L₄ (Figures 2, 3Q–R; Supplementary Table S2) occur in the middle and upper part of the Asselian stage, respectively, indicating the #L₃ and #L₄ limestones were deposited during the Asselian stage (Shen et al., 2019). The FO of the conodont *Sweetognathus aff. whitei* in limestone #L₈ (Figures 2, 3T,U; Supplementary Table S2) occurs at the base of the Artinskian stage and can be used to define the Sakmarian–Artinskian boundary (Shen et al., 2019).

4.2 Th/U, Al/Si and K/Si ratios, and weathering index of parker

Analyses of results from Th/U, Al/Si and K/Si ratios, and WIP are shown in Figure 4 and Supplementary Tables S3 and S4. Th/U ratios vary from 0.95 to 5.82 (mean (\bar{x}) = 4.2) (Supplementary Table S3), indicating little or no effect from depositional recycling on the samples. This is because recycled mudrocks exhibit high Th/U ratios of around 6 due to oxidation of U⁴⁺ to U⁶⁺ and its removal through the solution (Bhatia and

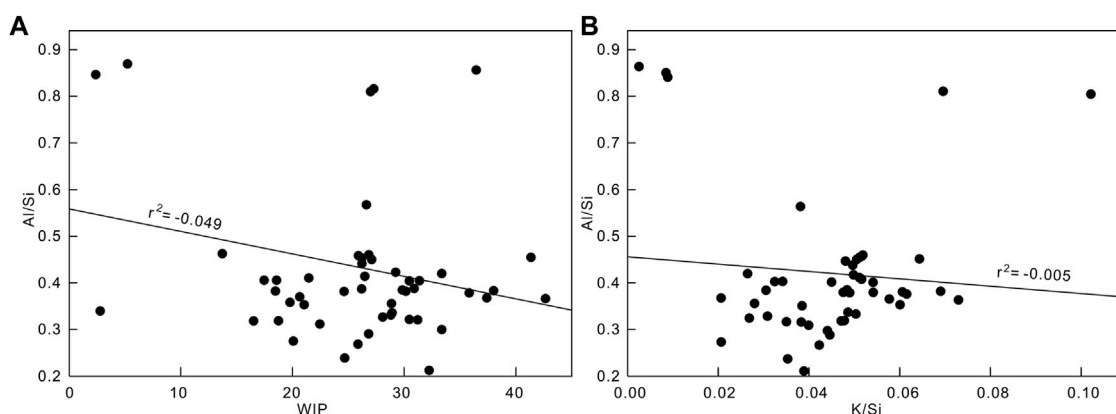


FIGURE 4

Plots of Al/Si ratio vs. weathering index of Parker (WIP) (A) and K/Si (B) showing no significant sedimentary sorting effect on sample compositions.

Taylor, 1981; Lu et al., 2020). Combined with the stable uplift of the provenance area (Liu, 1990) and the relative stability of source rock lithologies (Zhou, 2002), we exclude the influence of re-cycling on kaolinite content.

Al/Si ratios vary from 0.21 to 0.91 (\bar{x} = 0.43), K/Si ratios vary from 0.002 to 0.102 (\bar{x} = 0.044), and WIP varies from 2.40 to 42.64 (\bar{x} = 25.92). The poor correlation of Al/Si ratios with K/Si ratios (r^2 = -0.005, p < 0.01, n = 50) and WIP (r^2 = -0.049, p < 0.01, n = 50) (Figure 4, Supplementary Table S4) indicates that clay mineral compositions as weathering products are not controlled by hydraulic or sedimentary sorting processes (Yang et al., 2016, 2018).

4.3 Clay mineral composition, kaolinite, and micromorphology of kaolinite

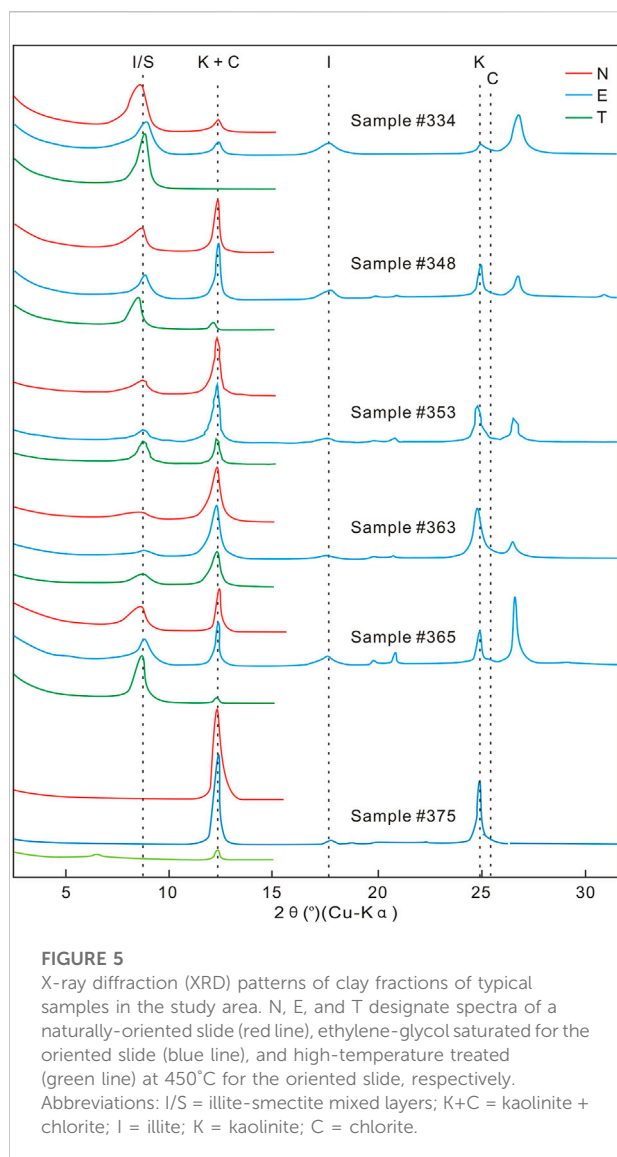
Results of clay mineral composition analysis, KI, and micromorphology of kaolinite are shown in Figures 2, 5, 6 and Supplementary Table S3. Clay minerals mainly consist of illite-smectite mixed layers (0–65%, \bar{x} = 41.7%) and kaolinite (19–67%, \bar{x} = 39.0%), followed by illite (1–35%, \bar{x} = 13.1%) and chlorite (0–21%, \bar{x} = 6.2%) (Figures 2, 5). Variations in kaolinite content allow the succession to be divided into six stages in ascending order (S-I to S-VI; Figure 2). Three higher value intervals of kaolinite content occur in the Benxi Formation (S-I; \bar{x} = 62.3%), the middle part of the Dajian to lower part of the Zhutougou members (S-III; \bar{x} = 53.3%), and the upper part of the Zhutougou (Taiyuan Formation) to the DZ & XT (Shanxi Formation) members (S-V; \bar{x} = 40.9%) (Figure 2). Three intervals with lower kaolinite content occur in the Dajian to lower part of the Mojie members (S-II; \bar{x} = 25.2%), the upper part of the Dajian to the lower part of the Zhutougou members (S-IV; \bar{x} = 27.7%), and the Xiaozhi Mudrock members (S-VI; \bar{x} = 22.0%) (Figure 2).

KI values vary from 0.22 to 1.88 $\Delta^\circ/2\theta$ (\bar{x} = 0.49 $\Delta^\circ/2\theta$), indicating that the mudrock samples were not affected by diagenesis (Cheng et al., 2019). The micromorphology of kaolinite mostly presents irregular fragments with sizes of 1–5 μm under the SEM (Figure 6), which is different from the authigenic kaolinite with vermiform and accordion-shaped morphologies formed during the diagenetic stage (Bauluz et al., 2008). This indicates the kaolinite of this study is of detrital origin, which is consistent with findings of the previous studies in the study area (Yang and Lei, 1987).

5 Discussion

5.1 Stratigraphic correlation and division

Recent zircon dating of tuffs and tuffaceous claystone in the NCP demonstrates that C-P lithostratigraphic units are widely diachronous (Figure 7) (Yang et al., 2020; Lu et al., 2021a; Wu et al., 2021). In the middle of the NCP, the C-P boundary occurs in the middle of the Taiyuan Formation in the Palougou section of Baode county (Wu et al., 2021) and the Shimenzhai section in the Liujiang Coalfield (Lu et al., 2021a), but in the Wuda Coalfield, the C-P boundary occurs near the top of the Taiyuan Formation (Figure 7) (Schmitz et al., 2020). The Taiyuan Formation is more than 180 m thick in Wuda but is much thinner in Baode (80 m) and Liujiang (75 m) (Figure 7). Similarly, the Asselian stage in the Palougou section includes four lithostratigraphic units and comprises the upper part of the Taiyuan Formation to the lower part of the Shangshihezi Formation (Figure 7) (Wu et al., 2021), but at Yongcheng in Henan Province, only the upper part of the Taiyuan Formation is assigned to the Asselian stage based on high-resolution Zircon dating (Figure 7) (Yang et al., 2020).



In the NCP, fossil plant biostratigraphy is well-developed and comprises distinct floral assemblages from the Taiyuan (*Neuropteris pseudovata*-*Lepidodendron posthumii* assemblage), Shanxi (*Emplectopteris triangularis*-*Emplectopteridium alatum*-*Lobatannularia sinensis* assemblage), Xiashihezi (*Cathaysiopteris whitei*-*Tingia carbonica* assemblage), and Shangshihezi (*Gigantonoclea lagreliei*-*Fasciapteris hallei*-*Lobatannularia heianensis* assemblage) formations (Wang, 2010; Yang and Wang, 2012). These fossil plant assemblages are correlated with the well-known plant assemblages in Europe, which were previously restricted to the Asselian–Capitanian stages (Wang, 2010; Yang and Wang, 2012; Liu et al., 2015). However, a new chronostratigraphic framework for the Permian succession of the NCP presented by Wu et al. (2021) infers that the well-established fossil plant and spore-pollen (palynological)

assemblages from the Taiyuan to Shangshihezi formations are also diachronous with the distinct floral assemblages tracking depositional environments through time and space (Figure 7). In this context, it is now necessary to synthesize radiometric age data with biostratigraphic (including conodonts and fusulinid fossils, but not necessarily fossil plants and palynology) and chemostratigraphic ($\delta^{13}\text{C}_{\text{org}}$ pattern) data from multiple sections across the NCP to further refine its stratigraphic framework.

Detailed biostratigraphic studies have previously been undertaken in the study area using conodonts, fusulinid, and plant fossils (Wang and Shang, 1989; Wang and Qi, 2003; Pei, 2004, 2009; Gao et al., 2005; Yang and Wang, 2012) from which we now consider the marine schemes (conodonts and fusulinids) more robust than fossil plant data. In the study area, the Taiyuan Formation was previously considered to be of the Asselian–Artinskian age based on the presence of the *Lepidodendron szeianum*-*L. Neuropteris ovata* fossil plant assemblage (Yang, 2006; Yang and Wang, 2012) and the fusulinids *Sphaeroschwagerina* and *Pseudoschwagerina* in limestone #L₁ (Yang and Lei, 1987; Wang and Shang, 1989; Wang and Qi, 2003; Pei, 2004, 2009; Gao et al., 2005). Combined with the first appearance datum (FAD) of the conodont *Streptognathodus isolatus* in limestone #L₁ (Figures 2, 3) in this study, this constrains the position of the C-P boundary to the top of the Benxi Formation in the Yuzhou Coalfield. This is based on the FAD of the conodont *S. isolatus* in the C-P boundary transition from the southern Urals in Russia that has been precisely calibrated by geochronological methods (298.92 ± 0.19 Ma) (Ramezani et al., 2007; Ramezani and Bowring, 2018). Similarly, the FAD of inflated fusulines such as *Sphaeroschwagerina* and *Pseudoschwagerina* that occurred in the middle and upper parts of the Maping and Chuanshan formations in South China and the lower part of the Taiyuan Formation in North China are close to the base of the Permian (Shen et al., 2019). This conclusion is further supported by the $\delta^{13}\text{C}_{\text{org}}$ chemostratigraphic correlation from the base of the Taiyuan Formation that indicates the position of the C-P boundary in the Yuzhou Coalfield (Lu et al., 2021c).

Zircon dating results in the Yongcheng Coalfield constraining the position of the Asselian–Sakmarian boundary to the top of the Taiyuan Formation and coincides with a change in conodont genera from *Streptognathodus* to *Sweetognathus* (Figure 7) (Gao et al., 2005; Yang et al., 2020). Although we did not observe a change from *Streptognathodus* to *Sweetognathus* in the samples we prepared, previous studies have shown this occurs in the limestone #L₄ in the Yuzhou Coalfield (Figure 2) (Wang and Zhang, 1985; Ding and Wan, 1990; Wang and Qi, 2003; Pei, 2004, 2009). Similarly, the FAD of the conodont *Streptognathodus cristellaris* in limestone #L₃ and *S. constrictus* in limestone #L₄ in this study (Figures 2, 3) indicate

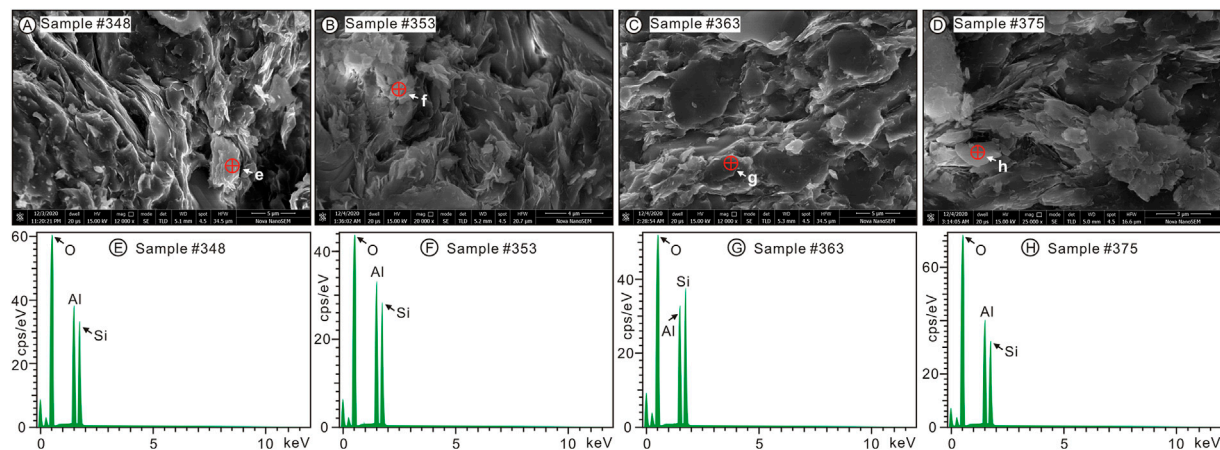


FIGURE 6
SEM images and spectra of the amorphous component of kaolinite from mudrock in the study area. (A–D), SEM images of mudrock samples #348, #353, #363, and #375 showing kaolinite is mostly irregular fragments with sizes of 1–5 mm, which is distinct from authigenic kaolinite that occurs as vermicular and accordion shaped particles in the diagenetic stage, reflecting the detrital origin of kaolinite in the studied strata; (E–H), spectra of the amorphous component of the kaolinite from samples #348, #353, #363, and #375.

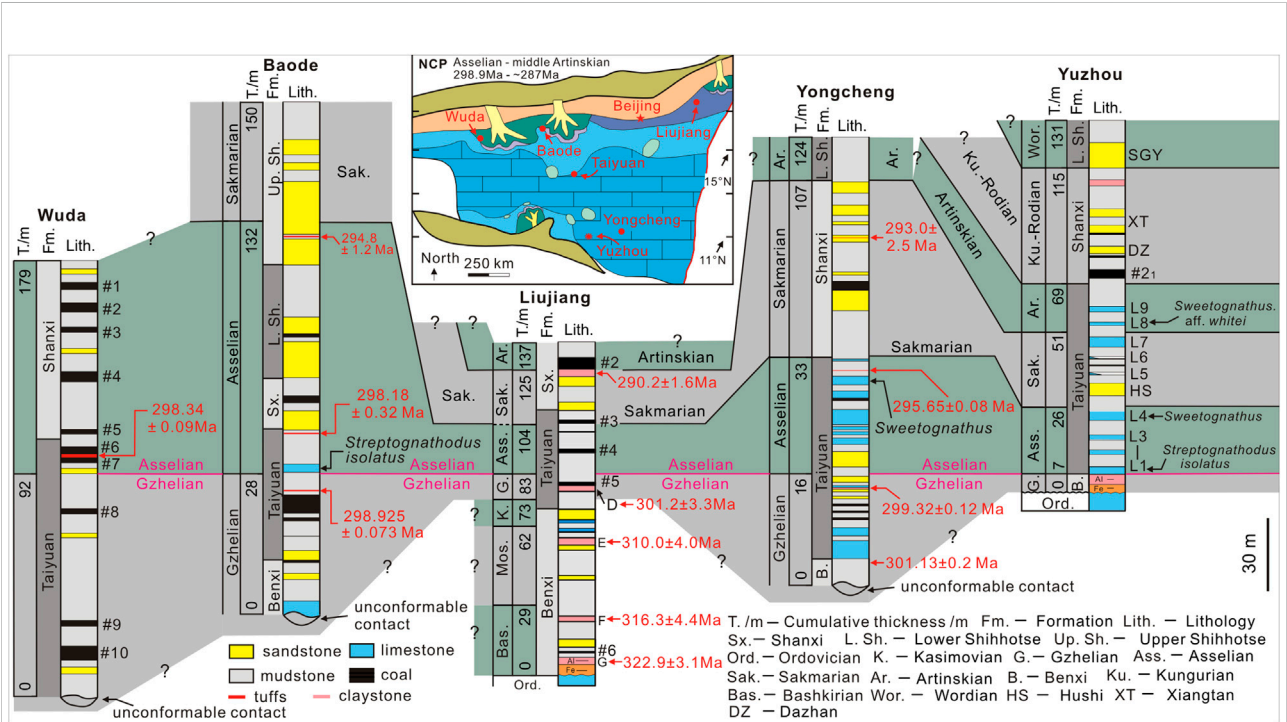
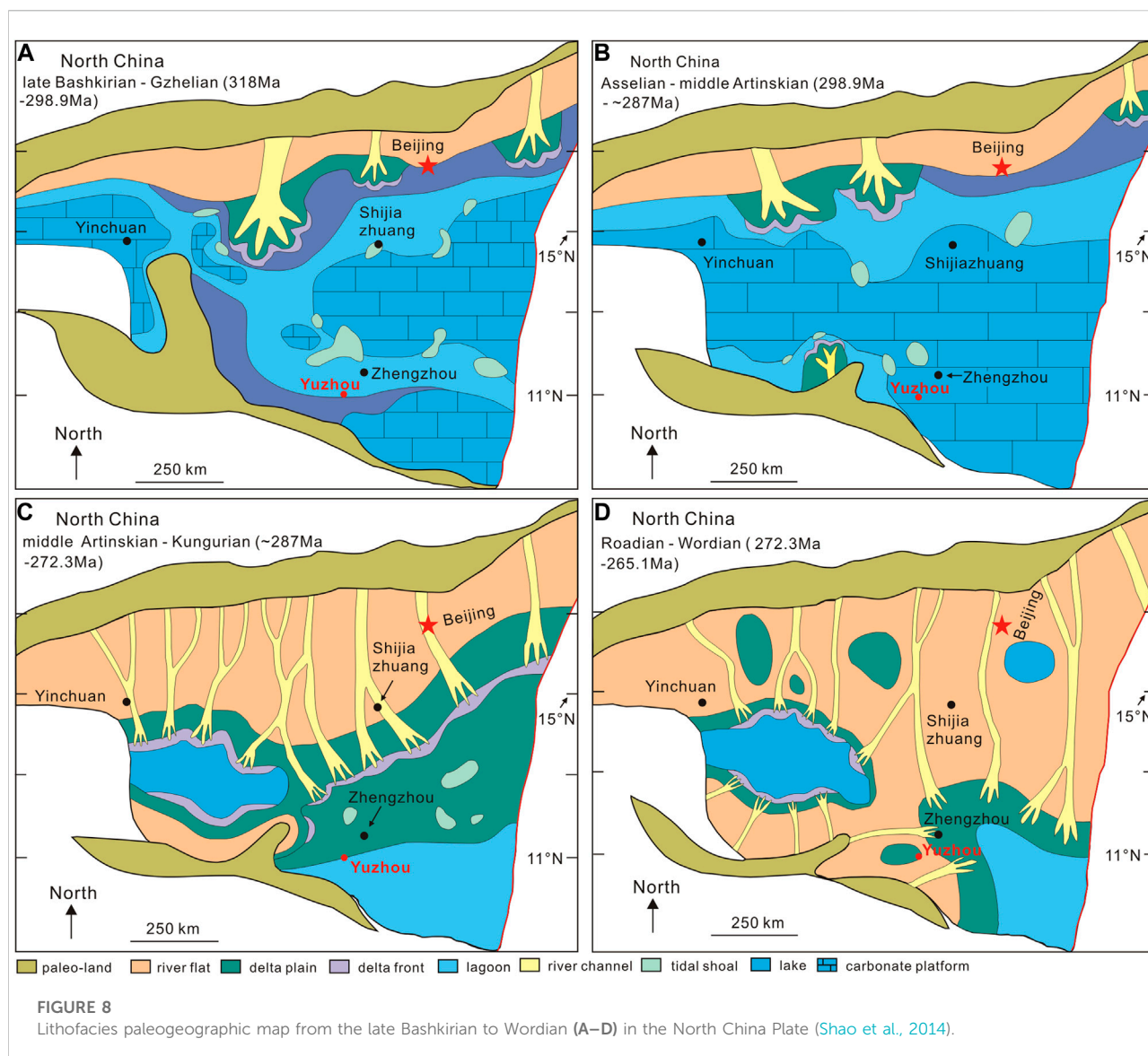


FIGURE 7
Chronostratigraphic and lithostratigraphic correlation of Carboniferous and Permian in the North China Plate (NCP). Lithology and age data of the sections at Wuda (Schmitz et al., 2020), Baode (Wu et al., 2021), and Liujiang (Lu et al., 2021a) and unpublished data, Yongcheng (Yang et al., 2020) and Yuzhou (this study) organized from north to south on the NCP during the Late Pennsylvanian to the earliest Guadalupian. Lithofacies paleogeographic map of the NCP modified from (Shao et al., 2014).



that limestones #L₃ and #L₄ are of Asselian age and place the base of the Sakmarian stage above limestone #L₄ (Figures 2, 7). This conclusion is based on the FO of the conodont *S. constrictus* and a change in conodont genera from *Streptognathodus* to *Sweetognathus* in the southern Urals that occurred in the late Asselian (Chernykh, 2006; Shen et al., 2019). Furthermore, $\delta^{13}\text{C}_{\text{org}}$ chemostratigraphy correlation from the middle part of the Taiyuan Formation in the Yuzhou Coalfield provides further evidence of a Sakmarian age (Lu et al., 2021c).

In our study, the FAD of the conodont *Sweetognathus* aff. *Whitei* in limestone #L₈ (Figures 2, 3) allows us to place the base of the Artinskian stage between limestones #L₇ and #L₈ (Figures 2, 7). This is based on the FAD of the conodont *S. aff. Whitei* in the southern Urals in a precisely calibrated geochronological framework that represents the base of the

Artinskian (290.10 ± 0.07 Ma) (Schmitz and Davydov, 2012). Furthermore, $\delta^{13}\text{C}_{\text{org}}$ chemostratigraphy from the upper part of the Taiyuan Formation in the Yuzhou Coalfield further supports the presence of an Artinskian age (Lu et al., 2021c).

The Shanxi Formation was previously considered to be of Kungurian–Roadian age based on the presence of the *Emplectopteris triangularis*–*Lobatannularia sinensis*–*Emplectopteridium alatum*–*Cathaysiopteris whitei* fossil plant assemblage (Figure 1C) (Yang, 2006; Yang and Wang, 2012). $\delta^{13}\text{C}_{\text{org}}$ chemostratigraphic correlation from the Shanxi Formation in the Yuzhou Coalfield provides further evidence of a Kungurian–Roadian age, of which the Xiaozhi Mudrock member is very close to the age of the Kungurian–Roadian boundary (Lu et al., 2021c). As a result, we roughly assign the Xiaozhi Mudrock

member to the Roadian stage and the remaining parts of the Shanxi Formation to the Kungurian stage.

Recent studies based on new high-resolution CA-ID-TIMS zircon U-Pb dating show that there is a ~20 Ma hiatus from approx. 280–260 Ma during the Cisuralian–Guadalupian transition in the northern NCP (Wu et al., 2021). This regional unconformity has also been documented in eastern Xinjiang (Yang et al., 2010) and in Inner Mongolia (Tang and Yan, 1993). The unconformity is related to uplift and erosion of the middle segment of the southern margin of the Paleo-Asian Ocean (PAO) caused by arc-continent and retro-arc fold-thrust deformation or the final closure of the PAO resulting from continental collision (*ca.* 280–265 Ma) (Xiao et al., 2018; Zhao et al., 2018). In the Yuzhou Coalfield on the southern NCP, there is no evidence of an unconformity in the Taiyuan and Shanxi formations (Yang and Lei, 1987; Yang and Wang, 2012; Lu et al., 2021c), and $\delta^{13}\text{C}_{\text{org}}$ patterns in the Yuzhou Coalfield are consistent with the global carbon cycle fluctuations during the Kungurian–Roadian interval (Cisuralian–Guadalupian transition) (Lu et al., 2021c). Therefore, we consider that the sedimentary strata in the Yuzhou Coalfield were continuous from 280 to 268 Ma. A similar situation occurs in the Longkou section of the Ordos Basin in the northern NCP, which also lacks an unconformity and experienced continuous deposition from 280 to 266 Ma (Wang et al., 2022). The unconformity and depositional hiatus are restricted to the northern part of the NCP and do not affect our study.

5.2 Low-latitude NCP climate change linked to the high-latitude glaciation

Changes in continental plate position, land-sea distributions, ice extent in Gondwana, atmospheric CO_2 , and monsoonal rainfall are considered the main factors controlling climate change in low latitudes during the LPIA (Tabor and Poulsen, 2008). In the study area, local paleomagnetic data demonstrate that no large-scale plate motion occurred from the early to late Early Permian (Supplementary Table S1) (Zhu et al., 1996). Through this time interval, the study area remained in an equatorial humid climate zone (Zhu et al., 1996) on the southern margin of the NCP in proximity to the sea (Figure 8). Following regression of the epicontinental sea in the middle Early Permian (Figures 8A,B), sedimentary environments gradually developed from coastal tidal flat and peat swamps to shallow-water deltaic environments (Figures 8C,D) (Yang and Lei, 1987; Zhu et al., 1996; Shang, 1997; Shao et al., 2014). Fossil plants were widespread and abundant, comprising stable, tropical, and ever-wet communities dominated by lycophytes, equisetophytes, marattialean ferns, and pteridosperms (Yang and Lei, 1987; Zhu et al., 1996; Yang, 2006; Hilton and Cleal, 2007).

Collectively, this information builds a picture of stable continental plate position and land-sea distributions. Paleoclimate studies in the NCP provide no evidence of monsoons during the early Permian (Yang and Lei, 1987; Shang, 1997; Yang and Wang, 2012). Consequently, we consider that the waxing and waning of ice sheets in high-latitude Gondwana and global changes in atmospheric $p\text{CO}_2$ were the main drivers for climate change in the study area through the LPIA.

In North China, substantial greenhouse gas emissions (e.g., CO_2 and CH_4) have driven global warming, resulting in the enhancement of global atmospheric circulation and the hydrological cycle and causing the widespread transition from dry to more humid conditions (Lu et al., 2021b). However, during the LPIA, the growth and decay of ice sheets in high-latitude Gondwana had a significant impact on the hydrological cycle, weathering rates, and climate in the low latitudes by influencing large-scale atmospheric circulation patterns and controlling migration of the Intertropical Convergence Zone (ITCZ) (Cecil et al., 2003; Tabor and Poulsen, 2008). The ITCZ is thought to have fluctuated strongly in response to the glaciations to nonglacial rhythms during the LPIA (Cecil et al., 2003; Tabor and Poulsen, 2008). Expansion of Gondwanan ice sheets during glaciation intervals compressed the ITCZ to a thin band near the equator, generating a wet climatic belt over tropical Pangea with increased annual rainfall. Conversely, the reduction of ice mass during nonglacial intervals caused the polar high-pressure cells to diminish, leading to an expanded ITCZ band and stronger seasonal excursions and resulting in reduced annual rainfall in the tropics (Cecil et al., 2003; Tabor and Poulsen, 2008).

In this study, kaolinite comprises irregular 1–5 μm sized fragments (Figure 6), indicating it is of detrital origin and is significantly different from authigenic kaolinite formed in well-drained and heavy leaching conditions or the alteration of volcanic ash (e.g., Bauluz et al., 2008). Detrital kaolinite in mudstones represents a component of fine-grained clastic sediment brought by rivers from terrigenous regions and is usually the product of intense chemical weathering of aluminosilicate (mainly feldspar and mica) minerals in terrigenous parent rocks and soils (e.g., Wang, 1989; Song et al., 2018). Furthermore, stable uplift of the provenance area (Liu, 1990) and the relative stability of source rock lithologies (Zhou, 2002) suggest that the kaolinite is not affected by the influence of tectonic activity in the provenance area or lithologic change of parent rock (e.g., Wang, 1989; Chen et al., 2003). The results from our study also show that kaolinite composition is not obviously affected by the influence of depositional recycling, hydraulic sorting, and post-deposition diagenesis (see Sections 4.2 and 4.3). Therefore, we conclude that the detrital kaolinite in the studied strata is a reliable proxy for paleoclimate reconstruction (e.g., Song et al., 2018) and that paleoclimate (especially changes in temperature and humidity) is the main

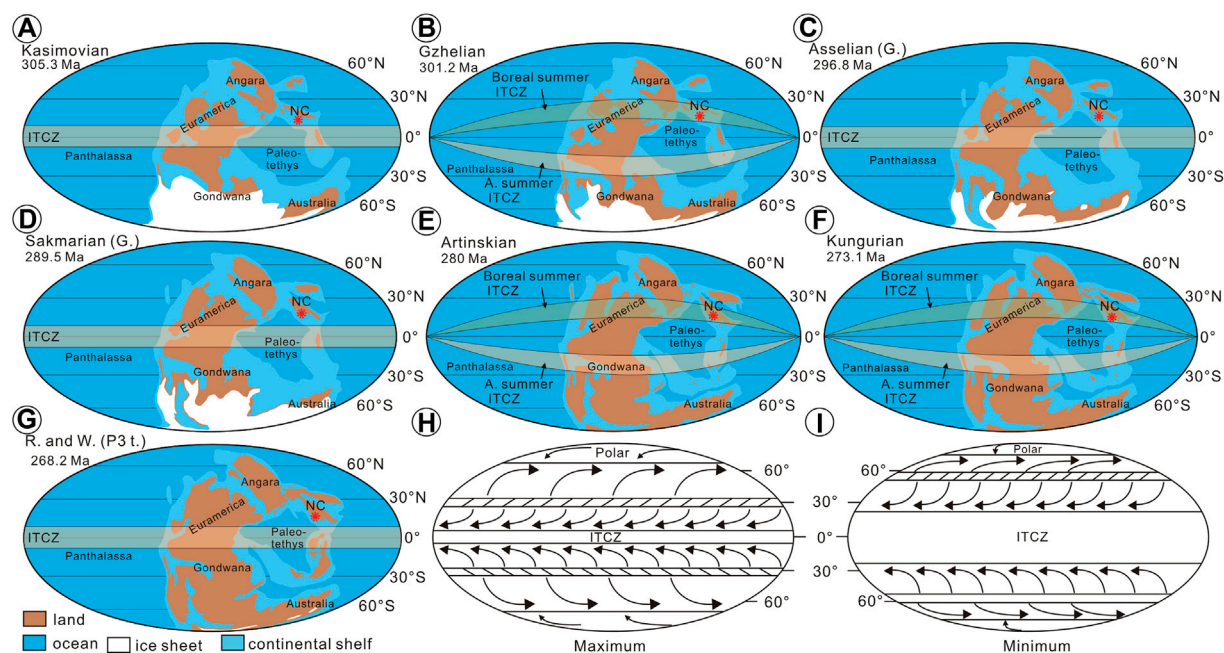


FIGURE 9

Global paleogeographic maps from the Kasimovian stage of the Carboniferous to the Wordian stage of the Permian (A–G) superimposed by Hadley circulation patterns for glacial maximum (H) and glacial minimum (I) conditions [modified from Tabor and Poulsen (2008)]. Base maps modified from Scotese and Wright (2018) (<http://www.earthbyte.org/paleodem-resource/scotese-and-wright-2018/>). Abbreviations: G. = Glaciation; R. and W. (P3 t.) = Roadian and Wordian (Glacier P3 transition); NC = North China; ITCZ = Intertropical Convergence Zone.

factor controlling variations in kaolinite content in the terrestrial Yuzhou Coalfield.

In this study, the change of detrital kaolinite content is mainly affected by relative temperature. Previous studies have shown that a large amount of detrital kaolinite can be formed by the reaction of aluminosilicate minerals (mainly feldspar and mica) with atmospheric temperature ($p\text{CO}_2$) and water (e.g., Wang, 1989). Under hot and humid climate conditions, wetland vegetation may develop and surface water is acidic, which is conducive to the decomposition of aluminosilicate minerals in parent rocks into kaolinite, increasing the content of detrital kaolinite in the resultant sediments (e.g., Wang, 1989). Conversely, under cool and dry climate conditions, the content of detrital kaolinite decreased (e.g., Wang, 1989). Given that the study area was in an equatorial zone and under humid climates with abundant peat formation and wetland plants through the early Permian (Zhu et al., 1996; Hilton and Cleal, 2007; Yang and Wang, 2012; Yang et al., 2016) and the large number of organic acids released in the decomposition process of plant residues and organic matter, those provide suitable conditions for the formation of kaolinite. However, in this study, kaolinite shows an alternating change trend in the ascending order, including a decreasing trend in the glacial period and an increasing trend in the nonglacial period, which means that the change of temperature (CO_2) in the glacial

period and nonglacial period may be the reason for change of kaolinite content (Figures 2, 9, 10). Evaluating detailed global paleogeographic maps from 305.3 to 268.2 Ma superimposed with Hadley circulation patterns for glacial maximum and minimum conditions (Figure 9) (Tabor and Poulsen, 2008) provides further insights into the effects of climate change on the study area. According to results from paleoclimate simulations (Tabor and Poulsen, 2008), the study area should have been affected by ITCZ compression during the Asselian–early Sakmarian, the late Sakmarian–early Artinskian, and the Roadian glaciations (Figures 9C,D, 10), with this associated with increased annual precipitation. Furthermore, the study area also should have been affected by seasonal ITCZ expansion from the Gzhelian nonglacial interval and two nonglacial intervals during the middle Sakmarian and middle Artinskian–Kungurian stages, with this associated with decreased annual precipitation (Figures 9E–G, 10, 11). However, in our study, the changing trend of weathering rates indicated by kaolinite content is inversely related to the simulated and predicted annual precipitation (Figures 9–11). Therefore, we consider that the change of kaolinite content in the study area is mainly affected by the change in global temperature during the non-glacial and glacial intervals. This is because, under humid climate conditions through the early Permian in the NCP, more hot climate conditions promoted the dissolution of Si ions in aluminum-

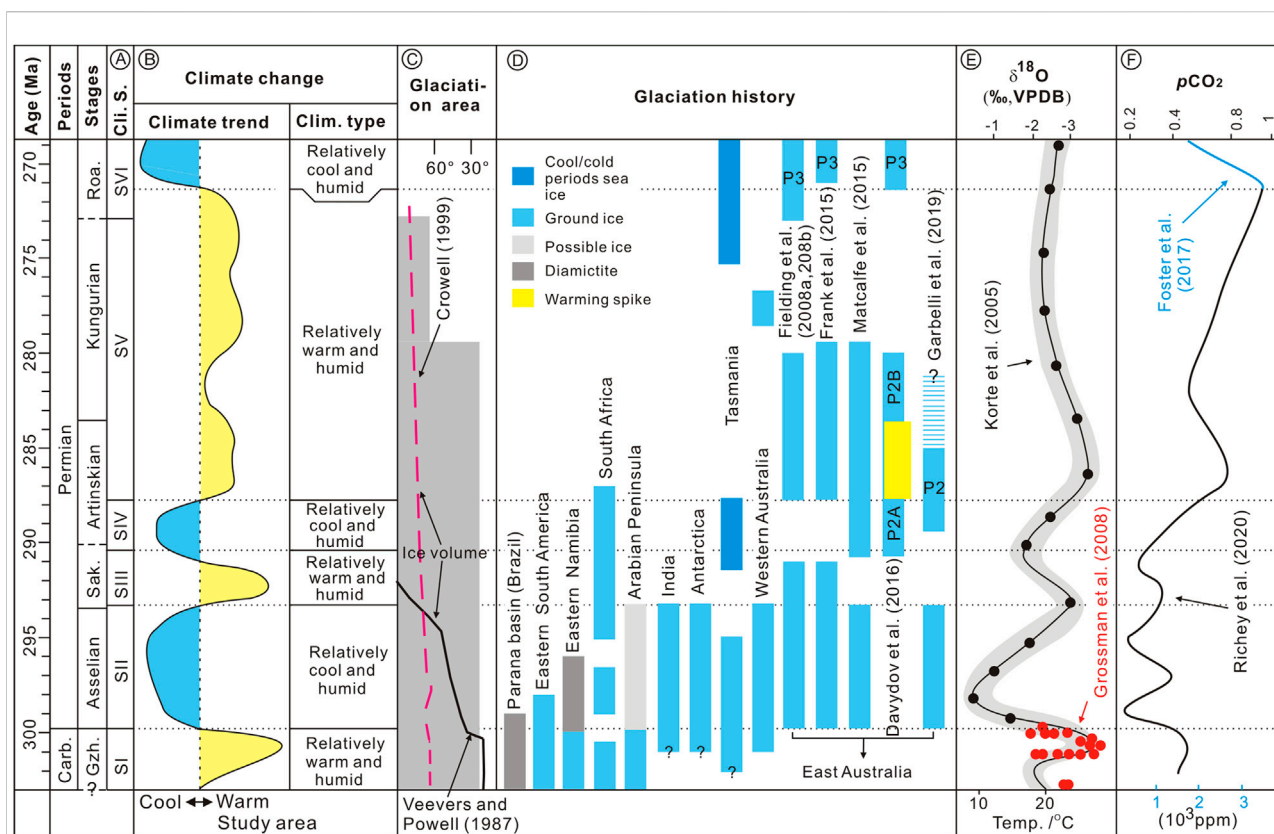


FIGURE 10

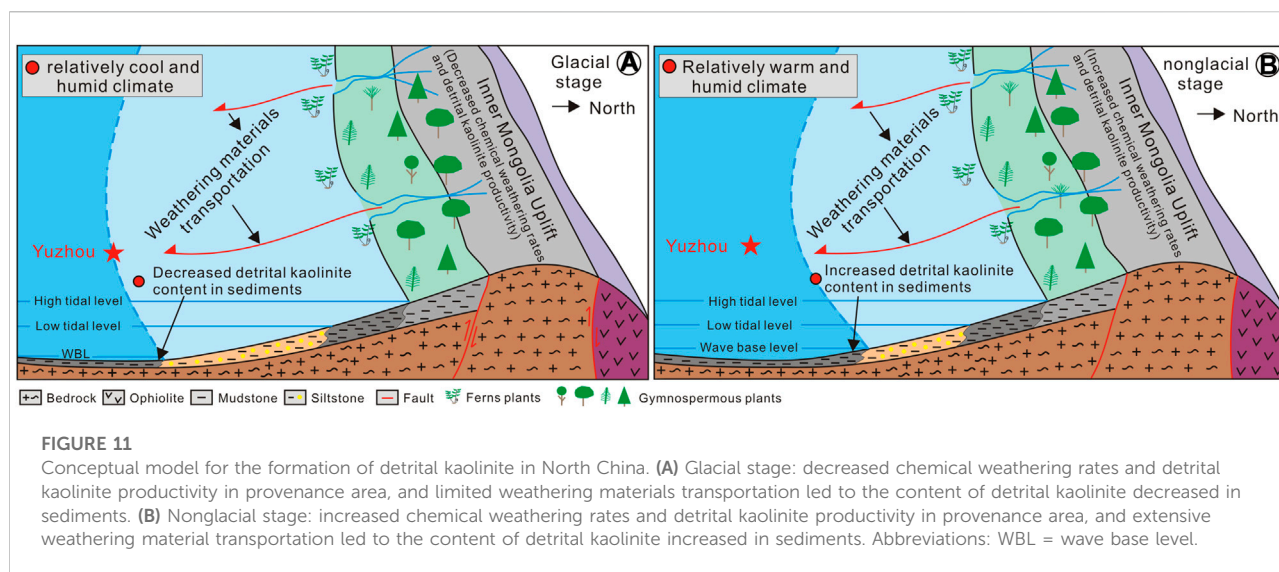
Comparison of climate change, glaciations, $\delta^{18}\text{O}$, and $p\text{CO}_2$ records from the Gzhelian Stage of the Carboniferous to the Roadian Stage of the Permian. Age stratigraphic framework from (Shen et al., 2019) (A), climate stages interpreted from the studied section (B), interpreted climatic records with blue representing intervals of climate cooling, while yellow represents climatic warming based on fluctuating climate signals from kaolinite content from the studied section and climate type interpreted from the studied section. (C) Glaciation area (modified after (Montañez and Poulsen, 2013) and (Griffis et al., 2018)) superimposed on glaciation area are relative ice-volume curves through time from (Veevers and Powell, 1987) (black line) and (Crowell, 1999) (red line). (D) Glaciation history modified from (Fielding et al., 2008a, 2008b, 2008c; Frank et al., 2008a, 2008b, 2015; Montañez and Poulsen, 2013; Metcalfe et al., 2015; Davydov et al., 2016; Griffis et al., 2018; Garbelli et al., 2019). (E) Oxygen isotope values from (Korte et al., 2005; Grossman et al., 2008). (F) Global $p\text{CO}_2$ concentration from (Foster et al., 2017; Richey et al., 2020). Abbreviations: Gzh. = Gzhelian; Sak. = Sakmarian; Cli. S. = climate stage; Clim. type = climate type; S. hemi. (E. Aus.) = Southern hemisphere including Eastern Australia; 2₁# = Coal 2₁ seam; Temp. = Temperature.

rich weathering products (Figure 6), which provided suitable conditions for the formation of detrital kaolinite, leading to rapid increase of kaolinite content during the nonglacial interval (Figure 11). On the contrary, kaolinite content decreased during the glacial interval (Figure 11). This also indicates that in the low-latitude NCP, relatively cool-humid climates prevailed during glacial intervals and warm-humid climates prevailed during nonglacial intervals (Figure 10).

During the Gzhelian (S-I), the kaolinite content increased rapidly, indicating a rapid increase in temperature in the NCP (Figures 2, 10). This is consistent with deglaciation in high-latitude Gondwana and global warming, which may have been caused by an increase in global atmospheric $p\text{CO}_2$ concentration caused by volcanism (Richey et al., 2020; Lu et al., 2021a; 2021c). During the Gzhelian, ice centers may have existed in the Kalahari Basin, the Karoo Basin, and possibly India and the eastern

Arabian Peninsula, but continental ice was absent from southwestern and south-central Gondwana (Parana Basin, Brazil; ~302–298 Ma) (Griffis et al., 2018) and eastern Gondwana (Australia) (Fielding et al., 2008a, 2008c, 2008b; Frank et al., 2008b, 2015). Furthermore, there was a significant increase in foraminifer diversity globally (Groves and Yue, 2009) and significant reductions in oxygen isotope values (Grossman et al., 2008), indicating a rise in global temperature during this time.

Glacial–nonglacial transitions are associated with especially large and rapid changes in climate conditions that can be readily recorded by bulk sediment composition (Frings, 2019; Wang et al., 2020). In this study, kaolinite content decreases rapidly at the onset and increases rapidly at the end of S-II (Figures 2, 10), indicating a rapid decrease and increase in temperatures, respectively. This is consistent with the rapid expansion and contraction of ice sheets



including sea ice accumulated in southern Gondwana at high latitudes (Griffis et al., 2018).

The rapid decrease in kaolinite content near the C-P boundary indicates rapid climate cooling in the NCP (Figure 2) and is also recorded by the continental Chemical Index of Alteration (CIA) in the Yongcheng Coalfield (Yang et al., 2020). This episode of climatic cooling was consistent with widespread early Permian ice sheet accumulation, including sea ice in high southern latitudes (including Antarctica, South America, South Africa, Arabian Peninsula, India, East Australia, and Western Australia) (Figure 10) (Fielding et al., 2008a, 2008b, 2008c; Frank et al., 2008b; Mory et al., 2008; Holz et al., 2010; Griffis et al., 2018). Climatic cooling at this time has been attributed to the decrease of $p\text{CO}_2$ caused by the re-expansion of paleotropical rainforests in equatorial Cathaysia (Cleal and Thomas, 2005) and/or the rapid post-eruptional weathering of the vast basaltic rocks of the Skagerrak-Centered large igneous province in tropical latitudes (Yang et al., 2020).

The rapid increase in kaolinite content during the mid-Sakmarian indicates rapid climate warming in the NCP (Figure 2). Similar rapid climate change has been recorded by the CIA and Mineralogical Index of Alteration (MIA) in the Karoo, Kalahari, and Khalaspir Basin of south Gondwana, where it has been interpreted as a marker for the onset of ice sheet retreat (Scheffler et al., 2006; Roy and Roser, 2013). During the mid-Sakmarian, glaciers disappeared in most basins in Gondwana and near Antarctica (Figure 10) (Griffis et al., 2018), but glacier P1 in eastern Australia may still have persisted (Fielding et al., 2008a, 2008c, 2008b; Frank et al., 2008a, 2008b, 2015).

Evidence supporting the large-scale loss of the ice sheet in high-latitude Gondwana in the mid-Sakmarian includes 1) marine transgression in low latitudes during the middle and late

Sakmarian (Montañez et al., 2007; Stemmerik, 2008; Koch and Frank, 2011); 2) prevalence of arid and semi-arid climates in the western Pangea (Poulsen et al., 2007; Montañez and Poulsen, 2013); 3) reduction in the extent and diversity of cold-water brachiopod faunas as temperatures increased in east Australia and New Zealand (Clapham and James, 2008; Waterhouse and Shi, 2010); and 4) latitudinal gradients of global brachiopod biodiversity returning to pre-LPIA levels (Powell, 2007). Although it is widely agreed that large-scale loss of ice sheet area in high-latitude Gondwana occurred during the mid-Sakmarian (Isbell et al., 2003; Montañez et al., 2007; Holz et al., 2010; Montañez and Poulsen, 2013; Liu et al., 2017; Griffis et al., 2018), the $p\text{CO}_2$ threshold for ice sheet ablation is controversial during this time interval. Estimates predict either $p\text{CO}_2$ increased significantly and was as high as 1,000–2,500 ppm (Figure 10) (Montañez et al., 2007) or experienced a more limited rise and was as low as 300–400 ppm (Figure 10) (Richey et al., 2020). Collectively, these may suggest that the $p\text{CO}_2$ threshold for ice sheet ablation was even lower than modeled (560 ppm) (Lowry et al., 2014) during the LPIA. This has been related to the lowering of the equatorial Hercynian mountains that led to a re-establishment of thick soils, while the assembly of Pangaea promoted arid conditions in continental interiors that were unfavorable for silicate weathering, causing $p\text{CO}_2$ to rise to levels sufficient to terminate the glacial event (Goddéris et al., 2017). Although the continental silicate weathering rates may have reduced because of the Hercynian mountain lowering and arid conditions, increasing $p\text{CO}_2$ might have been delayed due to increased burial of organic carbon preferentially in the ocean at this time (Chen et al., 2018; Richey et al., 2020).

During the Roadian stage, a significant decrease in kaolinite content in the study area (Figure 2) also was recorded in the Xikou Section and was interpreted to be related to the glacial

P3 in high-latitude eastern Australia (Cheng et al., 2019). The latest study has confined glacial P3 to the late Wordian-early Capitanian based on brachiopod shell-based $^{87}\text{Sr}/^{86}\text{Sr}$ calibration (Garbelli et al., 2019). However, $\delta^{18}\text{O}_{\text{apatite}}$ values from South China and North America show a positive shift from early Roadian to early Wordian (Chen et al., 2013; Shen et al., 2020), suggesting that Roadian climatic cooling recorded in the study area represents the climate transition to glacial P3 in high-latitude eastern Australia (Shen et al., 2020).

6 Conclusion

- 1) Combined conodont, fusulinid, and plant fossil biostratigraphy and lithostratigraphy provide a refined stratigraphic framework for the latest Carboniferous and early Permian strata in the Yuzhou Coalfield. This allows us to assign the Benxi, Taiyuan, and Shanxi formations in the Yuzhou coalfield to the Gzhelian, Asselian-Artinskian, and Kungurian-Roadian stages, respectively, and demonstrates the diachronous nature of the Carboniferous and early Permian lithostratigraphic formations in the NCP.
- 2) In the studied section, kaolinite is of terrigenous detrital origin and is not obviously affected by the influence of depositional recycling, hydraulic sorting, and post-deposition diagenesis, suggesting kaolinite is a reliable proxy for paleoclimate reconstruction. Kaolinite contents vary through succession and present alternating cool-humid and warm-humid climate conditions. These climatic conditions at low latitudes recorded high-latitude Gondwana glaciation events during the Asselian-early Sakmarian and the late Sakmarian-early Artinskian and the climatic transition to glacial P3 during the Roadian.
- 3) Two short-duration intervals with rapid climate change indicated by the changes in kaolinite content at the C-P boundary and in the mid-Sakmarian correspond with the onset of the early Permian peak icehouse conditions and permanent deglaciation, respectively. These imply that the Gondwana glaciation during the Asselian-middle Sakmarian was characterized by rapid expansion and rapid contraction.

Data availability statement

The original contributions presented in the study are included in the article/Supplementary Material; further inquiries can be directed to the corresponding author.

Author contributions

PZ, JL, MY, LS, and JH designed research. JL, PZ, MY, LS, ZW, and JH analyzed data. PZ, JL, MY, LS, and JH wrote the

manuscript. All co-authors contributed to the interpretation of the data and to the final manuscript.

Funding

This study has been supported by the National Key Research and Development Program of China (2021YFC2902000), the National Natural Science Foundation of China (Grant no. 42172196, 41472131, and 41772161), the National Science and Technology Major Project (Award no. 2017ZX05009-002), and the New Century Excellent Talents Fund of Chinese Ministry of Education (Award no. 2013102050020).

Acknowledgments

We are grateful to Fang Zhang for help in the identification of conodonts data, Suping Peng and Shifeng Dai (China University of Mining and Technology Beijing), Isabel Montañez, William DiMichele, Ahmed Radwan, and Christopher Fielding for comments on earlier versions of the manuscript and Pengju Li and Linsong Liu for discussions on clay minerals. We thank Idoia Rosales, Miguel Ángel Caja Rodríguez, and Neil Griffiths for their constructive and helpful comments on the manuscript.

Conflict of interest

MY was employed by PetroChina.

The remaining authors declare that the research was conducted in the absence of any commercial or financial relationships that could be construed as a potential conflict of interest.

Publisher's note

All claims expressed in this article are solely those of the authors and do not necessarily represent those of their affiliated organizations, or those of the publisher, the editors, and the reviewers. Any product that may be evaluated in this article, or claim that may be made by its manufacturer, is not guaranteed or endorsed by the publisher.

Supplementary material

The Supplementary Material for this article can be found online at: <https://www.frontiersin.org/articles/10.3389/feart.2022.956861/full#supplementary-material>

References

- Bauluz, B., Mayayo, M. J., Yuste, A., and González López, J. M. (2008). Genesis of kaolinite from albian sedimentary deposits of the iberian range (NE Spain): Analysis by XRD, SEM and TEM. *Clay Min.* 43, 459–475. doi:10.1180/claymin.2008.043.3.10
- Bhatia, M. R., and Taylor, S. R. (1981). Trace-element geochemistry and sedimentary provinces: a study from the tasman geosyncline, australia. *Chem. Geol.* 33, 115–125. doi:10.1016/0009-2541(81)90089-9
- Bishop, J. W., Montañez, I. P., and Osleger, D. A. (2010). Dynamic carboniferous climate change, arrow canyon, nevada. *Geosph. (Boulder)*. 6, 1–34. doi:10.1130/GES00192.1
- Cecil, C. B., Dulong, F. T., West, R. R., Stamm, R., Wardlaw, B., and Edgar, N. T. (2003). “Climate controls on the stratigraphy of a middle pennsylvanian cyclothem in North America,” in *Climate controls on Stratigraphy*. Editors C. B. Cecil and N. T. Edgar (Boulder, Colorado: SPEM Society for Sedimentary Geology), 151–180. doi:10.2110/pec.03.77.0151
- Chen, B., Joachimski, M. M., Shen, S., Lambert, L. L., Lai, X., Wang, X., et al. (2013). Permian ice volume and palaeoclimate history: Oxygen isotope proxies revisited. *Gondwana Res.* 24, 77–89. doi:10.1016/j.gr.2012.07.007
- Chen, J., Montañez, I. P., Qi, Y., Shen, S., and Wang, X. (2018). Strontium and carbon isotopic evidence for decoupling of $p\text{CO}_2$ from continental weathering at the apex of the late Paleozoic glaciation. *Geology* 46, 395–398. doi:10.1130/G40093.1
- Chen, T., Wang, H., Zhang, Z., and Wang, H. J. (2003). Clay minerals as indicators of paleoclimate. *Acta Pet. Mineral.* 22, 416–505. doi:10.3969/j.issn.1000-6524.2003.z1.022
- Cheng, C., Li, S., Xie, X., Cao, T., Manger, W. L., and Busbey, A. B. (2019). Permian carbon isotope and clay mineral records from the Xikou section, Zhen'an, shaanxi province, central china: climatological implications for the easternmost Paleo-Tethys. *Palaeogeogr. Palaeoclimatol. Palaeoecol.* 514, 407–422. doi:10.1016/j.palaeo.2018.10.023
- Chernykh, V. V. (2006). *Lower permian conodonts in the Urals*. Ekaterinburg: Institute of Geology and Geochemistry, Uralian Branch of the Russian Academy of Sciences. 130.
- Clapham, M. E., and James, N. P. (2008). Paleocology of early-middle permian marine communities in eastern australia: response to global climate change in the aftermath of the late paleozoic ice age. *Palaios* 23, 738–750. doi:10.2110/palo.2008.p08-022r
- Cleal, C. J., and Thomas, B. A. (2005). Paleozoic tropical rainforests and their effect on global climates: is the past the key to the present? *Geobiology* 3, 13–31. doi:10.1111/j.1472-4669.2005.00043.x
- Crowell, J. C. (1999). Pre-mesozoic ice ages: their bearing on understanding the climate system. *Pre-Mesozoic Ice Ages Their Bear. Underst. Clim. Syst.* 192, 106. doi:10.1130/0-8137-1192-4.1
- Davydov, V. I., and Biakov, A. S. (2015). Discovery of shallow-marine biofacies conodonts in a bioherm within the carboniferous–permian transition in the omolon massif, NE russia near the north paleo-pole: correlation with a warming spike in the southern hemisphere. *Gondwana Res.* 28, 888–897. doi:10.1016/j.gr.2014.07.008
- Davydov, V. I., Biakov, A. S., Isbell, J. L., Crowley, J. L., Schmitz, M. D., and Vedernikov, I. L. (2016). Middle Permian U–Pb zircon ages of the “glacial” deposits of the atkan formation, ayan-yuryakh anticlinorium, magadan province, NE russia: their significance for global climatic interpretations. *Gondwana Res.* 38, 74–85. doi:10.1016/j.gr.2015.10.014
- Davydov, V. I., Haig, D. W., and McCartney, E. (2014). Latest carboniferous (late gzhelian) fusulinids from timor leste and their paleobiogeographic affinities. *J. Paleontol.* 88, 588–605. doi:10.1666/13-007
- DiMichele, W. A., Cecil, C. B., Montañez, I. P., and Falcon-Lang, H. J. (2010). Cyclic changes in Pennsylvanian paleoclimate and effects on floristic dynamics in tropical Pangaea. *Int. J. Coal Geol.* 83, 329–344. doi:10.1016/j.coal.2010.01.007
- DiMichele, W. A. (2014). Wetland-dryland vegetational dynamics in the Pennsylvanian ice age tropics. *Int. J. Plant Sci.* 175, 123–164. doi:10.1086/675235
- Ding, H., and Wan, S. (1990). The carboniferous-permian conodont event-stratigraphy in the south of the north China platform. *Cour. Forschungsinstitut Senckenb* 118, 131
- Fedorchuk, N. D., Isbell, J. L., Griffis, N. P., Montañez, I. P., Vesely, F. F., Iannuzzi, R., et al. (2019a). Origin of paleovalleys on the rio grande do sul shield (Brazil): Implications for the extent of late paleozoic glaciation in west-central Gondwana. *Palaeogeogr. Palaeoclimatol. Palaeoecol.* 531, 108738. doi:10.1016/j.palaeo.2018.04.013
- Fedorchuk, N. D., Isbell, J. L., Griffis, N. P., Vesely, F. F., Rosa, E. L. M., Montañez, I. P., et al. (2019b). Carboniferous glaciectonized sediments in the southernmost paraná basin, brazil: ice marginal dynamics and paleoclimate indicators. *Sediment. Geol.* 389, 54–72. doi:10.1016/j.sedgeo.2019.05.006
- Fielding, C. R., Frank, T. D., Birgenheier, L. P., Rygel, M. C., Jones, A. T., and Roberts, J. (2008a). Stratigraphic imprint of the late palaeozoic ice age in eastern Australia: a record of alternating glacial and nonglacial climate regime. *J. Geol. Soc. Lond.* 165, 129–140. doi:10.1144/0016-76492007-036
- Fielding, C. R., Frank, T. D., Birgenheier, L. P., Rygel, M. C., Jones, A. T., and Roberts, J. (2008b). “Stratigraphic record and facies associations of the late Paleozoic ice age in eastern Australia (New South Wales and Queensland),” in *Special paper 441: Resolving the late paleozoic ice age in time and space*. Editors C. R. Fielding, T. D. Frank, and J. L. Isbell (Boulder, Colorado: Geological Society of America), 41–57. doi:10.1130/2008.2441(03)
- Fielding, C. R., Frank, T. D., and Isbell, J. L. (2008c). The late Paleozoic ice age - a review of current understanding and synthesis of global climate patterns. *Spec. Pap. Geol. Soc. Am.* 441, 343–354. doi:10.1130/2008.2441(24)
- Foster, G. L., Royer, D. L., and Lunt, D. J. (2017). Future climate forcing potentially without precedent in the last 420 million years. *Nat. Commun.* 8, 14845. doi:10.1038/ncomms14845
- Frank, T. D., Birgenheier, L. P., Montañez, I. P., Fielding, C. R., and Rygel, M. C. (2008a). “Late Paleozoic climate dynamics revealed by comparison of ice-proximal stratigraphic and ice-distal isotopic records,” in *Special paper 441: Resolving the late paleozoic ice age in time and space*. Editors C. R. Fielding, T. D. Frank, and J. L. Isbell (Boulder, Colorado: Geological Society of America), 331–342. doi:10.1130/2008.2441(23)
- Frank, T. D., Shultis, A. I., and Fielding, C. R. (2015). Acme and demise of the late palaeozoic ice age: a view from the southeastern margin of Gondwana. *Palaeogeogr. Palaeoclimatol. Palaeoecol.* 418, 176–192. doi:10.1016/j.palaeo.2014.11.016
- Frank, T. D., Thomas, S. G., and Fielding, C. R. (2008b). On using carbon and oxygen isotope data from glendonites as paleoenvironmental proxies: a case study from the permian system of eastern australia. *J. Sediment. Res.* 78, 713–723. doi:10.2110/jsr.2008.081
- Frings, P. J. (2019). Palaeoweathering: How do weathering rates vary with climate? *Elements* 15, 259–265. doi:10.2138/gselements.15.4.259
- Gao, L., Ding, H., and Wan, X. (2005). Taxonomic revision of conodont *Sweetognathus* species in the uppermost Taiyuan Formation, Yuhuai basin and its significance. *Acta Micropalaeontologica Sin.* 22, 370–382. doi:10.3969/j.issn.1000-0674.2005.04.004
- Garbelli, C., Shen, S. Z., Immenhauser, A., Brand, U., Buhl, D., Wang, W. Q., et al. (2019). Timing of early and middle permian deglaciation of the southern hemisphere: brachiopod-based $^{87}\text{Sr}/^{86}\text{Sr}$ calibration. *Earth Planet. Sci. Lett.* 516, 122–135. doi:10.1016/j.epsl.2019.03.039
- Goddéris, Y., Donnadieu, Y., Carretier, S., Aretz, M., Dera, G., MacOuin, M., et al. (2017). Onset and ending of the late palaeozoic ice age triggered by tectonically paced rock weathering. *Nat. Geosci.* 10, 382–386. doi:10.1038/ngeo2931
- Griffis, N. P., Montañez, I., Mundil, R., Heron, D. Le, Dietrich, P., Kettler, C., et al. (2021). High-latitude ice and climate control on sediment supply across SW gondwana during the late carboniferous and early Permian. *GSA Bull.* 133, 2113–2124. doi:10.1130/B35852.1
- Griffis, N. P., Montañez, I. P., Fedorchuk, N., Isbell, J., Mundil, R., Vesely, F., et al. (2019). Isotopes to ice: constraining provenance of glacial deposits and ice centers in west-central Gondwana. *Palaeogeogr. Palaeoclimatol. Palaeoecol.* 531, 108745. doi:10.1016/j.palaeo.2018.04.020
- Griffis, N. P., Mundil, R., Montañez, I. P., Isbell, J., Fedorchuk, N., Vesely, F., et al. (2018). A new stratigraphic framework built on U–Pb single-zircon TIMS ages and implications for the timing of the penultimate icehouse (Paraná Basin, Brazil). *GSA Bull.* 130, 848–858. doi:10.1130/B31775.1
- Grossman, E. L., Yancey, T. E., Jones, T. E., Bruckschen, P., Chuvashov, B., Mazzullo, S. J., et al. (2008). Glaciation, aridification, and carbon sequestration in the permo-carboniferous: the isotopic record from low latitudes. *Palaeogeogr. Palaeoclimatol. Palaeoecol.* 268, 222–233. doi:10.1016/j.palaeo.2008.03.053
- Groves, J. R., and Yue, W. (2009). Foraminiferal diversification during the late paleozoic ice age. *Paleobiology* 35, 367–392. doi:10.1666/0094-8373-35.3.367
- Hilton, J., and Cleal, C. J. (2007). The relationship between eurasian and cathaysian tropical floras in the Late Paleozoic: Paleobiogeographical and palaeogeographical implications. *Earth. Sci. Rev.* 85, 85–116. doi:10.1016/j.earscirev.2007.07.003
- Holz, M., França, A. B., Souza, P. A., Iannuzzi, R., and Rohn, R. (2010). A stratigraphic chart of the late carboniferous/permian succession of the eastern

border of the paran basin, brazil, south america. *J. South Am. Earth Sci.* 29, 381–399. doi:10.1016/j.jsames.2009.04.004

Isbell, J. L., Miller, M. F., Wolfe, K. L., and Lenaker, P. A. (2003). “Timing of late paleozoic glaciation in gondwana: was glaciation responsible for the development of northern hemisphere cyclothem?” in *Extreme Depositional Environments: Mega End Members in Geologic Time*. Editors J. L. Isbell, M. F. Miller, K. L. Wolfe, and P. A. Lenaker (Boulder, Colorado: Geological Society of America), 5–24. doi:10.1130/0-8137-2370-1.5

Koch, J. T., and Frank, T. D. (2011). The Pennsylvanian–permian transition in the low-latitude carbonate record and the onset of major gondwanan glaciation. *Palaeogeogr. Palaeoclimatol. Palaeoecol.* 308, 362–372. doi:10.1016/j.palaeo.2011.05.041

Korte, C., Jasper, T., Kozur, H. W., and Veizer, J. (2005). $\delta^{18}\text{O}$ and $\delta^{13}\text{C}$ of permian brachiopods: a record of seawater evolution and continental glaciation. *Palaeogeogr. Palaeoclimatol. Palaeoecol.* 224, 333–351. doi:10.1016/j.palaeo.2005.03.015

Liu, C., Jarochowska, E., Du, Y., Vachard, D., and Munnecke, A. (2017). Stratigraphical and $\delta^{13}\text{C}$ records of Permo-Carboniferous platform carbonates, South China: responses to late paleozoic icehouse climate and icehouse–greenhouse transition. *Palaeogeogr. Palaeoclimatol. Palaeoecol.* 474, 113–129. doi:10.1016/j.palaeo.2016.07.038

Liu, F., Zhu, H., and Ouyang, S. (2015). Late pennsylvanian to wuchiapingian palynostratigraphy of the baode section in the ordos basin, north china. *J. Asian Earth Sci.* 111, 528–552. doi:10.1016/j.jseas.2015.06.013

Liu, G. (1990). Permo-carboniferous paleogeography and coal accumulation in north china and south china continental plates. *Int. J. Coal Geol.* 16, 179–180. doi:10.1016/0166-5162(90)90032-T

Liu, Y., Hu, Z., Gao, S., Gunther, D., Xu, J., Gao, C., et al. (2008). *In situ* analysis of major and trace elements of anhydrous minerals by LA-ICP-MS without applying an internal standard. *Chem. Geol.* 257, 34–43. doi:10.1016/j.chemgeo.2008.08.004

Lowry, D. P., Poulsen, C. J., Horton, D. E., Torsvik, T. H., and Pollard, D. (2014). Thresholds for Paleozoic ice sheet initiation. *Geology* 42, 627–630. doi:10.1130/G35615.1

Lu, J., Wang, Y., Yang, M., Shao, L., and Hilton, J. (2021a). Records of volcanism and organic carbon isotopic composition ($\delta^{13}\text{C}_{\text{org}}$) linked to changes in atmospheric $p\text{CO}_2$ and climate during the Pennsylvanian icehouse interval. *Chem. Geol.* 570, 120168. doi:10.1016/j.chemgeo.2021.120168

Lu, J., Zhang, P., Dal Corso, J., Yang, M., Wignall, P. B., Greene, S. E., et al. (2021b). Volcanically driven lacustrine ecosystem changes during the carnian pluvial episode (late triassic). *Proc. Natl. Acad. Sci. U. S. A.* 118, e2109895118. doi:10.1073/pnas.2109895118

Lu, J., Zhang, P., Yang, M., Shao, L., and Hilton, J. (2020). Continental records of organic carbon isotopic composition ($\delta^{13}\text{C}_{\text{org}}$), weathering, paleoclimate and wildfire linked to the End-Permian Mass Extinction. *Chem. Geol.* 558, 119764. doi:10.1016/j.chemgeo.2020.119764

Lu, J., Zhou, K., Yang, M., Zhang, P., Shao, L., and Hilton, J. (2021c). Records of organic carbon isotopic composition ($\delta^{13}\text{C}_{\text{org}}$) and volcanism linked to changes in atmospheric $p\text{CO}_2$ and climate during the late paleozoic icehouse. *Glob. Planet. Change* 207, 103654. doi:10.1016/j.gloplacha.2021.103654

Metcalfe, I., Crowley, J. L., Nicoll, R. S., and Schmitz, M. (2015). High-precision U–Pb CA–TIMS calibration of middle permian to lower triassic sequences, mass extinction and extreme climate-change in eastern australian gondwana. *Gondwana Res.* 28, 61–81. doi:10.1016/j.gr.2014.09.002

Michel, L. A., Tabor, N. J., Montaez, I. P., Schmitz, M. D., and Davydov, V. I. (2015). Chronostratigraphy and paleoclimatology of the lodve basin, france: evidence for a pan-tropical aridification event across the carboniferous–permian boundary. *Palaeogeogr. Palaeoclimatol. Palaeoecol.* 430, 118–131. doi:10.1016/j.palaeo.2015.03.020

Montaez, I. P., and Poulsen, C. J. (2013). The late paleozoic ice age: An evolving paradigm. *Annu. Rev. Earth Planet. Sci.* 41, 629–656. doi:10.1146/annurev.earth.031208.100118

Montaez, I. P., Tabor, N. J., Niemeier, D., DiMichele, W. A., Frank, T. D., Fielding, C. R., et al. (2007). CO_2 -Forced climate and vegetation instability during late paleozoic deglaciation. *Science* 315, 87–91. doi:10.1126/science.1134207

Mory, A. J., Redfern, J., and Martin, J. R. (2008). “A review of Permian–Carboniferous glacial deposits in Western Australia,” in *Special Paper 441: Resolving the Late Paleozoic Ice Age in Time and Space*. Editors C. R. Fielding, T. D. Frank, and J. L. Isbell (Boulder, Colorado: Geological Society of America), 29–40. doi:10.1130/2008.2441(02)

Pei, F. (2009). Stratigraphic subdivision and chronological correlation of the north China-type permo-carboniferous in Henan. *Acta Geol. Sin. Henan*, 21

Pei, F. (2004). The North china type permo-carboniferous fusulinid and conodont biostratigraphic units of Henan Province. *J. Stratigr.* 28, 344–353. doi:10.3969/j.issn.0253-4959.2004.04.011

Poulsen, C. J., Pollard, D., Montaez, I. P., and Rowley, D. (2007). Late Paleozoic tropical climate response to gondwanan deglaciation. *Geol.* 35, 771–774. doi:10.1130/G23841A.1

Powell, M. G. (2007). Latitudinal diversity gradients for brachiopod genera during late paleozoic time: links between climate, biogeography and evolutionary rates. *Glob. Ecol. Biogeogr.* 16, 519–528. doi:10.1111/j.1466-8238.2007.00300.x

Ramezani, J., and Bowring, S. A. (2018). Advances in numerical calibration of the permian timescale based on radioisotopic geochronology. *Geol. Soc. Lond. Spec. Publ.* 450, 51–60. doi:10.1144/SP450.17

Ramezani, J., Schmitz, M. D., Davydov, V. I., Bowering, S. A., Snyder, W. S., and Northrup, C. J. (2007). High-precision U–Pb zircon age constraints on the carboniferous–permian boundary in the southern urals stratotype. *Earth Planet. Sci. Lett.* 256, 244–257. doi:10.1016/j.epsl.2007.01.032

Richey, J. D., Montaez, I. P., Godderis, Y., Looy, C. V., Griffis, N. P., and DiMichele, W. A. (2020). Influence of temporally varying weatherability on CO_2 – climate coupling and ecosystem change in the late Paleozoic. *Clim. Past.* 16, 1759–1775. doi:10.5194/cp-16-1759-2020

Roy, D. K., and Roser, B. P. (2013). Climatic control on the composition of carboniferous–permian gondwana sediments, khalaspur basin, bangladesh. *Gondwana Res.* 23, 1163–1171. doi:10.1016/j.gr.2012.07.006

Scheffler, K., Buehmann, D., and Schwark, L. (2006). Analysis of late paleozoic glacial to postglacial sedimentary successions in south africa by geochemical proxies – response to climate evolution and sedimentary environment. *Palaeogeogr. Palaeoclimatol. Palaeoecol.* 240, 184–203. doi:10.1016/j.palaeo.2006.03.059

Schmitz, M. D., and Davydov, V. I. (2012). Quantitative radiometric and biostratigraphic calibration of the Pennsylvanian–Early Permian (Cisuralian) time scale and pan-Euramerican chronostratigraphic correlation. *Geol. Soc. Am. Bull.* 124, 549–577. doi:10.1130/B30385.1

Schmitz, M. D., Pfefferkorn, H. W., Shen, S. Z., and Wang, J. (2020). A volcanic tuff near the carboniferous–permian boundary, taiyuan formation, north China: radioisotopic dating and global correlation. *Rev. Palaeobot. Palynol.* 294. doi:10.1016/j.revpalbo.2020.104244

Scotese, C. R., and Wright, N. (2018). PALEOMAP paleodigital elevation models. Available at: <http://www.earthbyte.org/paleodem-resourcescotese-and-wright-2018/>.

Shang, G. (1997). *The late Paleozoic coal geology of North China Platform*. Taiyuan: Shanxi Science and Technology Press, 1–160.

Shao, L., Dong, D., Li, M., Wang, H., Wang, D., Lu, J., et al. (2014). Sequence-paleogeography and coal accumulation of the carboniferous–permian in the north China basin. *J. china* 39, 1725–1734. doi:10.13225/j.cnki.jccs.2013.9033

Shen, S., Yuan, D., Henderson, C. M., Wu, Q., Zhang, Y., Zhang, H., et al. (2020). Progress, problems and prospects: an overview of the Guadalupian series of South China and North America. *Earth. Sci. Rev.* 211, 103412. doi:10.1016/j.earscirev.2020.103412

Shen, S., Zhang, H., Zhang, Y., Yuan, D., Chen, B., He, W., et al. (2019). Permian integrative stratigraphy and timescale of China. *Sci. China Earth Sci.* 62, 154–188. doi:10.1007/s11430-017-9228-4

Singer, A. (1984). The paleoclimatic interpretation of clay minerals in sediments – a review. *Earth. Sci. Rev.* 21, 251–293. doi:10.1016/0012-8252(84)90055-2

Song, Y., Wang, Q., An, Z., Qiang, X., Dong, J., Chang, H., et al. (2018). Mid-miocene climatic optimum: clay mineral evidence from the red clay succession, longzhong basin, northern China. *Palaeogeogr. Palaeoclimatol. Palaeoecol.* 512, 46–55. doi:10.1016/j.palaeo.2017.10.001

Stemmerik, L. (2008). “Influence of late paleozoic Gondwana glaciations on the depositional evolution of the northern pangean shelf, north Greenland, svalbard, and the barents sea,” in *Special paper 441: Resolving the late paleozoic ice age in time and space*. Editors C. R. Fielding, T. D. Frank, and J. L. Isbell (Boulder, Colorado: Geological Society of America), 205–217. doi:10.1130/2008.2441(14)

Tabor, N. J., Montaez, I. P., Scotese, C. R., Poulsen, C. J., and Mack, G. H. (2008). “Paleosol archives of environmental and climatic history in paleotropical Western Pangea during the latest Pennsylvanian through Early Permian,” in *Special paper 441: Resolving the late paleozoic ice age in time and space*. Editors C. R. Fielding, T. D. Frank, and J. L. Isbell (Boulder, Colorado: Geological Society of America), 291–303. doi:10.1130/2008.2441(20)

Tabor, N. J., and Montaez, I. P. (2002). Shifts in late Paleozoic atmospheric circulation over Western equatorial Pangea: Insights from pedogenic mineral $\delta^{18}\text{O}$ compositions. *Geology* 30, 1127. doi:10.1130/0091-7613(2002)030<1127:SILPAC>2.0

- Tabor, N. J., and Poulsen, C. J. (2008). Palaeoclimate across the late pennsylvanian-early permian tropical palaeolatitudes: a review of climate indicators, their distribution, and relation to palaeophysiographic climate factors. *Palaeogeogr. Palaeoclimatol. Palaeoecol.* 268, 293–310. doi:10.1016/j.palaeo.2008.03.052
- Tang, K., and Yan, Z. (1993). Regional metamorphism and tectonic evolution of the inner mongolian suture zone. *J. Metamorph. Geol.* 11, 511–522. doi:10.1111/j.1525-1314.1993.tb00168.x
- Thiry, M. (2000). Palaeoclimatic interpretation of clay minerals in marine deposits: an outlook from the continental origin. *Earth. Sci. Rev.* 49, 201–221. doi:10.1016/S0012-8252(99)00054-9
- Veevers, J. J. t., and Powell, C. M. (1987). Late Paleozoic glacial episodes in gondwanaland reflected in transgressive-regressive depositional sequences in eurafrica. *Geol. Soc. Am. Bull.* 982, 475–487. doi:10.1130/0016-7606(1987)98<475:lpgeig>2.0.co;2
- Wang, J. (2010). Late paleozoic macrofloral assemblages from weibei coalfield, with reference to vegetational change through the late paleozoic ice-age in the north china block. *Int. J. Coal Geol.* 83, 292–317. doi:10.1016/j.coal.2009.10.007
- Wang, J., and Pfefferkorn, H. W. (2013). The Carboniferous-permian transition on the north china microcontinent-oceanic climate in the tropics. *Int. J. Coal Geol.* 119, 106–113. doi:10.1016/j.coal.2013.07.022
- Wang, P., Du, Y., Yu, W., Algeo, T. J., Zhou, Q., Xu, Y., et al. (2020). The chemical index of alteration (CIA) as a proxy for climate change during glacial-interglacial transitions in earth history. *Earth. Sci. Rev.* 201, 103032. doi:10.1016/j.earscirev.2019.103032
- Wang, X. (1989). Palaeoclimate significance of vertical variations of clastic kaolinite in mudstones, Hailaer Basin. *Min. Rocks* 9, 41–47. doi:10.19719/j.cnki.1001-6872.1989.03.007
- Wang, Y., Yang, S., Zhang, S., Huang, X., Sun, M., and Ding, Z. (2022). Early-middle permian drying in the north china block induced by large igneous provinces. *Palaeogeogr. Palaeoclimatol. Palaeoecol.* 592, 110922. doi:10.1016/j.palaeo.2022.110922
- Wang, Z., and Qi, Y. (2003). Review of carboniferous-permian conodont biostratigraphy in north China. *Acta Micropala eontologica Sin.* 20, 225. doi:10.3969/j.issn.1000-0674.2003.03.002
- Wang, Z., and Shang, G. (1989). A preliminary study on the carboniferous-permian strata in Dafengkou of the Yu county, Henan province. *J. Stratigr.* 13, 290–295. doi:10.19839/j.cnki.dcxz.1989.04.005
- Wang, Z. (1991). Conodonts from Carboniferous-Permian boundary strata in China with comments on the boundary. *Acta Palaeontol. Sin.* 30, 6–41. doi:10.19800/j.cnki.aps.1991.01.002
- Wang, Z., and Zhang, W. (1985). Discovery of conodonts from the upper part of the taiyuan formation in Yuxian, Henan. *J. Stratigr.* 9, 228
- Waterhouse, J. B., and Shi, G. R. (2010). Evolution in a cold climate. *Palaeogeogr. Palaeoclimatol. Palaeoecol.* 298, 17–30. doi:10.1016/j.palaeo.2010.08.022
- Wu, Q., Ramezani, J., Zhang, H., Wang, J., Zeng, F., Zhang, Y., et al. (2021). High-precision U-Pb age constraints on the permian floral turnovers, paleoclimate change, and tectonics of the North China block. *Geology* 49, 677–681. doi:10.1130/G48051.1
- Xiao, W., Windley, B. F., Han, C., Liu, W., Wan, B., Zhang, J., et al. (2018). Late Paleozoic to early triassic multiple roll-back and oroclinal bending of the Mongolia collage in Central Asia. *Earth. Sci. Rev.* 186, 94–128. doi:10.1016/j.earscirev.2017.09.020
- Yang, G. (2006). *The Permian cathaysian flora in western Henan province, China-Yuzhou flora*. Beijing: Geological Publishing House, 1–76.
- Yang, G. X., and Wang, H. S. (2012). Yuzhou flora-A hidden gem of the middle and late cathaysian flora. *Sci. China Earth Sci.* 55, 1601–1619. doi:10.1007/s11430-012-4476-2
- Yang, J., Cawood, P. A., Du, Y., Condon, D. J., Yan, J., Liu, J., et al. (2018). Early Wuchiapingian cooling linked to emeishan basaltic weathering? *Earth Planet. Sci. Lett.* 492, 102–111. doi:10.1016/j.epsl.2018.04.004
- Yang, J., Cawood, P. A., Du, Y., Li, W., and Yan, J. (2016). Reconstructing early permian tropical climates from chemical weathering indices. *Geol. Soc. Am. Bull.* 128, 739–751. doi:10.1130/B31371.1
- Yang, J., Cawood, P. A., Montañez, I. P., Condon, D. J., Du, Y., Yan, J., et al. (2020). Enhanced continental weathering and large igneous province induced climate warming at the permo-carboniferous transition. *Earth Planet. Sci. Lett.* 534, 116074. doi:10.1016/j.epsl.2020.116074
- Yang, Q., and Lei, S. (1987). *Depositional environments and coal-forming characteristics of late palaeozoic coal measures in Yuxian, Henan Province*. Beijing: Geological Publishing House, 1–70.
- Yang, W., Feng, Q., Liu, Y., Tabor, N., Miggins, D., Crowley, J. L., et al. (2010). Depositional environments and cyclo- and chronostratigraphy of uppermost carboniferous-lower triassic fluvial-lacustrine deposits, southern bogda mountains, NW China-a terrestrial paleoclimatic record of mid-latitude NE Pangea. *Glob. Planet. Change* 73, 15–113. doi:10.1016/j.gloplacha.2010.03.008
- Zhao, G., Wang, Y., Huang, B., Dong, Y., Li, S., Zhang, G., et al. (2018). Geological reconstructions of the east asian blocks: from the breakup of rodinia to the assembly of Pangea. *Earth. Sci. Rev.* 186, 262–286. doi:10.1016/j.earscirev.2018.10.003
- Zhou, A. (2002). *The evolution of late paleozoic basins in north margin of north china block and the coupling relationship between basin and range*. Beijing: China Coal Industry Publishing House, 1–157.
- Zhu, H., Yang, G., and Sheng, A. X. (1996). A study on palaeomagnetism of permian strata in the Dafengkou section, Yuzhou, Henan Province. *Acta Geol. Sin.* 70, 121
- Zhu, Z. Y., Jiang, S. Y., Liu, G. X., and Zhao, K. D. (2013). Precise dating of the middle permian: zircon U-Pb geochronology from volcanic ash beds in the basal gufeng formation, yangtze region, south china. *Gondwana Research* 23, 1599–1606. doi:10.1016/j.gr.2012.08.008